WAVEFRONT ENGINEERING TO IMAGE NEURO- AND VASO-MICRODYNAMICS THROUGHOUT MOUSE CORTEX

In "Illuminating the Depths: Advanced Technologies in Deep Brain Imaging Using Light and Sound", Lingyan Shi and Junjie Yao, editors.

Rishyashring R. Iyer
Department of Physics, University of California, San Diego, La Jolla, CA, USA

Pantong Yao
Department of Neurosciences, University of California, San Diego, La Jolla, CA, USA

Mikhail Drobizhev
Department of Microbiology and Cell Biology, Montana State University, Bozeman, MT, USA

Fatemeh Dehghan Nezhad
Department of Biomedical Science and Engineering, Gwangju Institute of Science and Technology, Gwangju, South Korea

Tien Nhat Nguyen
Department of Biomedical Science and Engineering, Gwangju Institute of Science and Technology, Gwangju, South Korea

Euiheon Chung
Department of Biomedical Science and Engineering, Gwangju Institute of Science and Technology, Gwangju, South Korea

David Kleinfeld
Department of Physics and Department of Neurobiology, University of California, San Diego, La Jolla, CA, USA

1. INTRODUCTION

Animal behavior exhibits remarkable complexity and adaptability, reflecting the diverse ways in which organisms interact with their environments. At the foundation of this diversity lies the nervous system, a sophisticated control architecture that generates motor commands while integrating sensory feedback to refine and adapt behavior. Through this continuous interplay of command and correction, the nervous system produces behaviors that are flexible and efficient. Deciphering these processes requires direct access to neural activity, strategies to decode the meaning of neural signals, and an analysis of the dynamics that govern interactions among signaling pathways.

Achieving access to neural activity requires methods that can resolve both neural action potentials and synaptic transmissions in the intact brain with cellular precision. Two-photon fluorescence microscopy provides this capability, offering high spatial resolution, optical sectioning, and stable *in vivo* recordings across multiple sessions or days. In the mouse, the combination of genetic accessibility and a rich behavioral repertoire makes two-photon imaging a powerful platform to study cortical computation, enabling direct observation of how neural activity is organized both across columns and through layers in the rodent cortex.

In this chapter, we discuss the fundamental limitations of two-photon microscopy for imaging deep cortical layers and how wavefront engineering enables imaging throughout the rodent cortex. In Section 2, we provide an overview of the mathematical principles underlying these limitations and introduce the components of a wavefront engineering system. The comprehensive step-by-step guide in Section 3 will enable readers to implement wavefront engineering within existing multiphoton microscopes in their laboratories to drive critical studies in cortical neural circuits.

1.1. What do people typically image? What modalities?

Within this framework, calcium imaging with genetically encoded indicators such as GCaMP has become the most widely adopted two-photon strategy, enabling the monitoring of neuronal activity across large populations with high spatial and temporal resolution (Chen et al. 2017; Ebrahimi et al. 2022; Manley et al. 2024). Action potentials can raise intracellular calcium concentration by 10- to 100-fold above baseline, producing strong fluorescence changes and yielding a high signal-to-noise ratio that makes even single spikes detectable (Chen et al. 2013; Zhang et al. 2023c). However, calcium signals are only a surrogate for action potentials. Calcium dynamics inherently cannot report subthreshold voltage changes within the cell, and their relatively slow kinetics limit temporal resolution, making it difficult to resolve high-frequency spiking or precise spike timing. Despite these constraints, the reliability and sensitivity of calcium imaging have established it as the workhorse of modern two-photon studies.

To overcome the limitations of calcium indicators, genetically encoded voltage indicators (GEVIs) provide a direct readout of membrane potential (Liu et al. 2022; Platisa et al. 2023; Hao et al. 2024). By operating on the millisecond timescale, GEVIs can resolve individual action potentials as well as subthreshold events. These events are voltage fluctuations that do not trigger action potentials but are critical for synaptic integration, dendritic computation, and shaping the nonlinear dynamics of neural circuits. Calcium imaging is effectively blind to these signals, leaving a substantial gap in our ability to study how neurons process input and transform them into output. Capturing such fast events requires two-photon imaging at kilohertz frame rates, which necessitates specialized system design and remains a substantial challenge for most laboratories (Kazemipour et al. 2019; Wu et al. 2020; Platisa et al. 2023) (see Section 1.4). In addition, GEVIs typically generate smaller fluorescence changes and lower signal-to-noise ratios than calcium indicators, making experiments technically demanding. Nevertheless, recent generations, including ASAP5/6, JEDI-2P, SpikeyGi2, have markedly improved in brightness, speed, and photostability (Liu et al. 2022; Platisa et al. 2023; Hao et al. 2024).

Genetically encoded neurotransmitter and neuromodulator sensors further extend the utility of two-photon neuroimaging. These sensors are designed to report the release of signaling molecules as fluorescence changes, enabling direct visualization of chemical communication *in vivo* (Sabatini and Tian 2020; Yang et al. 2024). The glutamate sensor, iGluSnFR, for example, provides a direct measure of excitatory synaptic input. Since its advent, iGluSnFRs have emerged a powerful tool for probing the input–output function of single neurons and, more broadly, for understanding cortical computation (Aggarwal et al. 2023). While action potentials can be tracked with millisecond precision using voltage indicators, neurotransmitter release is inherently slower, as it represents the essential step by which neurons influence one another. Neurotransmitter sensors therefore occupy a “sweet spot” between temporal resolution and signal-to-noise ratio: their signals are less temporally sharp than voltage indicators and therefore easier to detect, while also being more direct and interpretable than calcium imaging, especially at dendritic spines or boutons. Neuromodulator sensors such as GRAB-DA and dLight extend this approach to dopamine, while others target acetylcholine, serotonin, and norepinephrine, capturing modulatory dynamics that influence learning, motivation, and behavioral state over longer timescales (Patriarchi et al. 2018; Deng et al. 2024; Zhuo et al. 2024; Feng et al. 2024).

Two-photon microscopy has also been applied to longitudinal imaging of the structural dynamics of dendritic spines, axonal boutons, and other subcellular structures (Fu et al. 2012; Wright et al. 2025). Unlike functional indicators that capture rapid activity, structural imaging operates over days to weeks, allowing researchers to track synaptic growth, elimination, and remodeling with high spatial resolution. Chronic imaging through cranial windows has shown that dendritic spines undergo both rapid turnover and long-term stabilization, processes thought to underlie learning and memory. By linking fast functional dynamics to slow structural changes, structural imaging provides a powerful approach for studying plasticity on longer timescales.

In addition, vascular and metabolic imaging extend the scope of two-photon studies by linking neural activity to the brain's support systems of blood flow and energy metabolism (Kleinfeld et al. 2011; Nasu et al. 2023). Fluorescent labeling of blood plasma or red blood cells allows measurement of vessel diameter, red blood cell velocity, and capillary dynamics *in vivo*, providing detailed readouts of cerebral blood flow. Complementary approaches use genetically encoded sensors for metabolites (e.g., eLACCO2.1, iGlucoSnFR2) to monitor shifts in cellular energy usage at high spatial and temporal resolution. Together, these methods enable detailed investigation of neurovascular relationships and how they are reshaped across behavioral states and disease conditions.

While calcium signals are typically measured from the neuronal cell bodies (soma), new generations of calcium sensors have been used to image Ca^{2+} dynamics in specific dendritic branches too (Chen et al. 2013). Neuronal voltages are also typically imaged from the soma; however, since the GEVIs are expressed only along the cell membranes, the images only contain a thin outline of the cell, thereby restricting the signal-to-noise ratio considerably compared to Ca^{2+} imaging of the soma. Similarly, glutamate imaging captures dynamics within individual boutons or spines, each of which occupies only a few pixels in a diffraction-limited optical microscope. Imaging blood flow perhaps has the largest spatiotemporal range, given the large size difference between pial vessels and the highest branch order of capillaries, nearly two orders of magnitude. Thus, the demand for high spatial resolution exists regardless of the signal of interest in cortical imaging using multiphoton microscopy at depth.

Finally, the integration of two-photon imaging with optogenetic stimulation has enabled all-optical experiments, in which targeted neurons can be manipulated while activity is simultaneously recorded from the surrounding network (Papagiakoumou et al. 2010; Marshel et al. 2019; Adesnik and Abdeladim 2021; Russell et al. 2022). This combination allows precise testing of causal hypotheses about circuit function, bridging observation and intervention within the same experimental framework. Together, these methodological advances establish two-photon microscopy as a versatile and continually evolving platform for dissecting cortical computation across multiple spatial and temporal scales.

1.2. Why can't regular imaging methods work?

The neocortex is organized into a stereotyped laminar architecture of six layers that together form the canonical cortical column, often regarded as a fundamental computational unit (Harris and Shepherd 2015). Each layer contains distinct cell types and connectivity patterns that contribute to cortical processing in complementary ways. Layer 4 serves as the primary entry point for thalamic input, distributing sensory information into local circuits. Layer 5 contains large pyramidal neurons that project to subcortical structures, making it a major source of cortical output. Layer 6 provides feedback to both the thalamus and other cortical layers, regulating excitability and shaping recurrent dynamics. Despite the central importance of these deeper layers for input-output transformations, most two-photon imaging studies have concentrated on layers 2/3, where pyramidal neurons form dense horizontal connections and are readily accessible optically. This emphasis reflects the technical limitations of conventional two-photon microscopy, which suffers from scattering and sample-induced aberrations that degrade signal and resolution with depth, making stable imaging beyond ~300 µm in depth challenging to achieve *in vivo*. As a result, much of our high-resolution understanding of cortical dynamics comes from superficial layers, while the deeper circuits that drive input–output transformations remain comparatively underexplored.

The key obstacle to reaching these layers is the presence of optical aberrations, which arise when light traveling through brain tissue encounters variations in refractive index from cell membranes, organelles, or vasculature. These microscopic irregularities distort the wavefront of the excitation light, broadening the focal spot and reducing both resolution and signal intensity with depth. Adaptive optics (AO) provides a powerful solution by correcting these distortions in real time (Liu et al. 2019; Yao et al. 2023). In wavefront engineering, the incident light on the sample is reshaped using devices such as deformable mirrors or spatial light modulators, such that the light reconverges into a sharp focus at the intended depth even after propagating through scattering tissue (Section 2.4). AO extends two-photon imaging into deep layers by restoring both resolution and fluorescent signal levels, enabling direct investigation of computations across the full cortical column. Beyond imaging, wavefront engineering has also driven major advances in holographic two-photon stimulation, which uses patterned light to manipulate neuronal populations with single-cell precision. Although we focus on AO for imaging applications, readers interested in holographic stimulation are referred to recent comprehensive reviews (Adesnik and Abdeladim 2021; Russell et al. 2022; Emiliani et al. 2022).

1.4. Beam multiplexing for faster dynamic imaging

With next-generation sensors now offering sub-millisecond response times, there is an urgent need for fast high-throughput optophysiology tools to advance data-driven cortical circuit research. Existing methods for accelerating multiphoton microscopy include scan rate multiplication units and beam multiplexing techniques (**Figure 1**). In this section, we provide a brief overview of how the various multiplexing techniques enhance imaging speed and throughput in multiphoton microscopy.

Scan rate multiplication units (SMUs) increases the scanning rate of two-photon microscopy using lenslet arrays (**Figure 1A**). A single scan on a lens will yield a line at the focal plane. However, since lenslet arrays have multiple optical axes, a single scan over a lenslet array creates multiple shorter lines at the focal plane. Displacing the optical axes of the lenslets produces multiple spatially displaced short lines for a single scan across the lenslet array. Xiao et al. showed that an array of 16 lenslets can multiply a 16 kHz scan rate to 256 kHz (Xiao et al. 2021). Typical multiphoton lasers are Titanium-Sapphire based and operate at 80 MHz, corresponding to 1 pulse every 12.5 nanoseconds. Since the fluorescence lifetime of GFP-based fluorophores is 3-4 ns, there is potential to “copy” each laser pulse into several copies displaced in space and time, a strategy known as beam multiplexing. Platisa et al. implemented their SMURF (spatiotemporal multiplexed ultrafast resonance frame-scanning) microscope (Platisa et al. 2023) by manually creating four temporally-displaced copies of the original pulse, which were spatially displaced as two copies each (**Figure 1D**). The eight resulting beamlets were demultiplexed using a line detector (PMT array). The field-of-view multiplication is fixed; more copies would require complete redesign of the microscope. Second, neither the multiplication unit nor the detection can be easily incorporated into existing setups without major optical modifications. In another beam multiplexing method called spectro-temporal laser imaging by diffractive excitation (SLIDE), the laser spectrum is split into multiple spectral segments by an electro-optic modulator and directed to different parts of the sample using a diffractive element (Karpf et al. 2020) (**Figure 1G**). In this case, the signal-to-noise ratio of the images are affected since each pulse incident on a pixel is only a subset of the bandwidth of the laser.

Table 1. *Comparison of multiplexing techniques*

Technique	Enabling technology	Acceleration factor	Effective line rate	Field-of-view (equivalent at 1,000 fps)	Detection	Integra-tion with AO
A. Traditional 2P			0.016 MHz	256 × 16 px	PMT	
B. Scan rate multiplication unit	Lenslet array as tube lens to reset the optical axis	Acceleration by 2× number of lenslets; 74× in Xiao et al.	0.592 MHz	256 × 256 px	PMT	Not shown
C. Reverberation cavity	Cavity to offset the foci of beamlets	Axial multiplexing; 10× in Beaulieu et al.	200 MHz (axially)	900 µm axially, spaced 90 µm apart	PMT	No
D. SMURF	Beam splitters and beam combiners	Fixed at 8× Platisa et al.	128 kHz	320 × 192 px 800 fps	16× PMT array	No
E. FACED	Nearly parallel mirrors with cylindrical lens	80-200× (Wu et al.) Tunable by mirror tilt	1 MHz	900 × 80 px	PMT	No
F. Scanless multiphoton	Holographic excitation of specific regions	Accelerated by up to 15 cells of interest (Sims et al.)		15 cells	kHz CMOS camera	No
G. SLIDE	Spectrally narrow beamlets sent to sample points with a grating	Tunable using the EOM (Karpf et al.)	0.342 MHz	256 × 170 px	PMT	No
H. SLAP	4 line foci at 4 angles scanned sequentially	Accelerated by 1000x (line foci) (Sims et al.)		1000 × 1000 px	SiPM	No

With the development of ytterbium (Yb)-based lasers with a 1-20 MHz repetition rates, more beamlets can be “copied” between two laser pulses. Beaulieu et al. designed a microscope with a reverberation cavity in which the beam gains a slight “defocus” at each iteration of the cavity to create beamlet copies that focus to different axial planes in the sample (**Figure 1C**) (Beaulieu et al. 2020). While not necessarily a scan-multiplication setup, this configuration significantly accelerated volumetric imaging in the mouse brain.

Yb-based lasers have also been multiplexed using the FACED (free-space angular-chirp-enhanced delay) method, in which the beam is reflected between nearly parallel reflectors so that the output beams are spread in time and angularly separated as integer multiples of the angle between the two reflectors(**Figure 1E**) (Wu et al. 2016, 2020; Lai et al. 2021). This yields a line rate equivalent to the laser repetition rate of 1-2 MHz. Another approach to increase scan speeds is to restrict excitation to specific regions of interest. Sims et al. developed a scanless two-photon imaging method simultaneously excites only the regions of interest, for example, up to 15 cells within a plane, using a spatial-light modulator (**Figure 1F**) (Sims et al. 2024). Similarly, Kazemipour et al. demonstrated Scanned Line Angular Projection Microscopy (SLAP), which combines an electro-optic modulator and a spatial light modulator for projecting of four scanning lines across selected regions of interest (**Figure 1H**) (Kazemipour et al. 2019).

The methods described in this section may serve as possible extensions to the standard multiphoton microscope to utilize the advances in sensor design for neuroimaging applications. Nonetheless, these techniques do not address the issues with deeper imaging. The readers are encouraged to find intersections between these extensions and the adaptive optics methods presented in this chapter for both deeper and faster imaging using the same system.

2. PRINCIPLES

Here, we introduce the mathematical and instrumental basis for AO. Optical aberrations were a persistent problem, known to scientists like Ibn al-Haytham and Roger Bacon since the 11th-13th century, when the inability of a purely spherical lens to create a perfect focus was observed. However, much of the work in "aberration correction" up to the 18th century was dedicated to the correction of chromatic aberration, where the focal spots of different wavelengths of light are displaced along the optical axis. The complex series of equations by Euler, D'Alembert, Gauss, Clairaut, Herschel, and several other prominent scientists of the early 19th century were formalized and simplified by Hamilton's "quaternions; primarily to describe spherical aberrations (Clairaut 1762; Hamilton 1828; Herschel 1833; Johnson 1992; Ferlin 2017). Seidel provided the general mathematical notations for monochromatic aberrations up to the 5th order to describe the five most common like defocus, astigmatism, coma, field curvature, and distortions (Conrady 1918). Alongside these theoretical pursuits, experimental opticians like John Dollond, Joseph Lister, Andrew Ross, and James Smith utilized these concepts to devise chromatic and/or spherical aberration-free lenses (Prosser 1917). This historical brief was included to show that the initial approaches to understanding optical aberrations were fundamentally rooted in the geometry of the rays interacting with the surface of the optical elements. The equations, while rigid and thorough, were particularly cumbersome as the order of aberrations increased.

The application of Fourier transforms in optical physics, with the work of Abbe and Porter and later formalized by Pierre-Michel Duffieux, simplified numerous problems in the field, including aberrations (Duffieux 1983). Harold Hopkins utilized Fourier theory to describe the various orders of aberrations using the concept of "wavefronts", commonly described today using the orthogonal 2D-polynomials described by Fritz Zernike (Zernike 1934; Hopkins 1951).

2.1. Fourier Optics 101

A thorough understanding of Fourier optics and wavefront theory is critical for analyzing and correcting the optical aberrations in deep tissue microscopy. We outline three core concepts in Fourier optics that form the foundation for AO. While a complete treatment of image formation in Fourier optics requires both Fraunhofer (far-field) and Fresnel (near-field) diffraction equations, only the essential for aberration correction are presented here. Consider the optical system in Figure 2A using light of wavelength λ and wavenumber $k = 2\pi/\lambda$. The field at the object plane is $U_o(x,y)$. The field at a distance d from the optical element E, propagates, with a transfer function of $H_E(x,y,)$ and), forms an image at plane I at a distance $\bar{d}$ from E, with a field $U_i(\bar{x},\bar{y})$.

1) When the optical element E is an ideal lens with a focal length of f, $H_E(x,y)$ is a pure phase object described by

$$H(x,y) = \exp\left(-i\frac{k\left(x^2+y^2\right)}{2f}\right). \tag{1}$$

A key property of converging lenses is to collimate a point source placed at the focus. This is similar to the Fourier transform relationship between a Dirac delta function and the constant equal to 1. Within our model, only when $d = \bar{d} = f$, the optical field at the image plane is a scaled Fourier transform of the object plane field.

$$U_i(\bar{x},\bar{y}) = \frac{k}{i2\pi f} e^{2ikf}\,\widehat{U}_o\left(\frac{kx}{2\pi f}, \frac{ky}{2\pi f}\right), \tag{2}$$

where $\widehat{U}_o$ is the Fourier transform of U_o. Thus, the lens could be considered as an ideal Fourier transformer. This equation is the basis for several optical elements within a microscopy system. First, a telescope consisting of two lenses placed at a distance equal to the sum of their focal lengths apart is essentially an optical relay that translates the optical field at the front focal plane of the first lens to the back focal plane of the second lens. This arrangement of lenses is called the 4-f configuration. Second, a mirror placed at an angle θ between the two lenses at the intersection of their focal plane causes the image at the back focal plane of the second lens to the displaced by $f \cdot \tan(2\theta)$. This forms the basis of Galvanometric mirror scanners typically employed for raster scanning the beam at a fixed focal plane at the sample (see Figure 2B). Third, a pupil placed at the front focal plane will essentially act as a spatial low-pass filter for the field at the back focal plane. In a typical multiphoton microscope, the optical elements like spatial light modulators, galvanometer mirrors, deformable mirrors, and single-pixel detectors are typically placed in the Fourier plane of the sample (odd number of lenses between the sample plane and the plane of the element) where the beam is not spatially displaced. Multipixel detectors like cameras and point-spread function (PSF) conditioners like pinholes are placed in the conjugate sample plane (even number of lenses between the sample plane and the plane of the element).

2) The wavefront of the beam the focal plane on the sample is defined as the phase function at the Fourier plane. Typically, since most optical elements are transparent/reflective with spatially uniform profiles, the magnitude of the optical field is assumed to be constant. Therefore, any distortions to the beam at the sample plane can be modeled as purely phase changes to the wavefront. Similarly, optical aberrations are also modeled as a phase addition to the optical wavefront. In Figure 2A, the wavefront of $U_i(\bar{x},\bar{y})$, $W_i(\bar{x},\bar{y}) = \angle\widehat{U}_i(k_{\bar{x}},k_{\bar{y}})$, where $k_{\bar{x}}$ and $k_{\bar{y}}$ are the spatial frequency variables of $\bar{x}$ and $\bar{y}$. In thick biological tissues, the distortion to the focal plane from the superficial layers can be modelled as additions to the wavefront. The aberrated optical field, $U_a(x,y)$, at the focal plane can described be in terms of the unaberrated optical field, $U(x,y)$, and the aberration $\phi_a(k_x,k_y)$ as

$$U_a(x,y) = \mathcal{F}^{-1}_{k_x,k_y\to x,y}\left\{e^{\jmath\phi_a(k_x,k_y)}\cdot e^{\jmath W(k_x,k_y)}\right\} = \mathcal{F}^{-1}_{k_x,k_y\to x,y}\left\{e^{\jmath\phi_a(k_x,k_y)}\cdot \mathcal{F}_{x,y\to k_x,k_y}\{U(x,y)\}\right\}, \quad (3)$$

where $\mathcal{F}$ is the Fourier transform function and $|U(x,y)|$ is a constant (Figure 2C). In AO, the function of the deformable mirror is to negate the added phase with the spatially varying surface profile described by $z_{DM}(k_x,k_y)$. The corrected image field, $U_c(x,y)$, is described as

$$U_c(x,y) = e^{\jmath\frac{2\pi}{\lambda}z_{DM}(k_x,k_y)}U_a(x,y) \approx U(x,y), \quad (4)$$

which will approximate the unaberrated wavefront (Figure 2D). The pattern at the deformable mirror not only corrects for the sample-induced aberration but also corrects for imperfections within the optical system (called system AO). While the wavefront can, in theory, be estimated for each x,y location on the SHWFS that can be re-scaled for each piston on the DM, using an orthonormal basis function reduces the complexity of the problem.

2.2. Zernike modes

Zernike polynomials are a series of polynomial functions that are orthogonal on a unit circle, are hierarchical and intuitive to describe classical aberrations like defocus, astigmatism, coma, and spherical aberrations, and have a smooth modal representation. Figure 3 shows the first 20 Zernike polynomials and the corresponding

PSF at the sample plane. Z_0^0, Z_1^1, Z_1^{-1}, and Z_2^2 correspond to offset, horizontal tilt, vertical tilt, and defocus, which are ignored for any corrections. The practical utility of using these Zernike polynomials is described in Section 3.

2.3. The cause and effect of optical aberrations

Any scattering that occurs outside of the focal plane causes aberrations. Scattering occurs at the interface of media with different refractive indices. Consider a plane wavefront encountering a converging lens with a curved surface. The different parts of the wavefront are reshaped by the lens non-uniformly, where the rays near the periphery are more strongly focused compared to the center. Thus, the focal spot is less sharp than the ideal scenario, a phenomenon called spherical aberration. Similarly, imagine the lens center offset from the beam's optical axis: one side of the beam towards the center will be more strongly focused, creating a focus with coma aberration.

Biological tissues are optically heterogenous. The brain is comprised of cells with large protein content, blood vessels with highly refractile and moving red blood cells, and neuronal axons surrounded by myelin. There are also superficial brain layers, such as the dura mater, that the light encounters when imaging through a cranial window. Consequently, the type and severity of aberrations vary markedly across samples, imaging depths, and lateral field of view. The distortions worsen progressively with imaging depth.

These aberrations have two major effects. First, the profile of the incident beam becomes distorted at the focal plane, increasing the beam width far beyond the diffraction limit. In the Fourier plane, this corresponds to a relative decrease in the higher spatial frequencies, thereby degrading image resolution. In brain imaging, this leads to a loss of fine dendritic and synaptic detail and inaccurate measurements of capillary diameters in vascular studies. Second, in multiphoton microscopy, fluorescence intensity depends on the tightness of the focal spot; a broader focus decreases both signal strength and localization precision. This severely limits the ability to image fast cellular and sub-cellular dynamics at depth. Therefore, the metrics used to evaluate aberrations or the efficiency of adaptive correction must account for both overall intensity and the redistribution of intensity toward higher spatial frequencies. This will be discussed in Section 3.5.

2.4. Strategies for wavefront engineering in neurosciences

Having now established the significance of the Fourier plane to capture and modulate the wavefront, we discuss the strategies for wavefront actuation and sensing, focusing on widely used components like deformable mirrors and wavefront sensors (WFS). In these applications, researchers typically consider correction within an *isoplanatic patch* of approximately 50-100 µm, over which the aberration is assumed to be invariant.

2.4.1. Actuation strategies

Actuation strategies are electromechanical or electrooptic elements that physically modulate the wavefront of the illumination or detection light path to impose phase corrections by dynamically adjusting their shape or refractive properties. Two primary actuation devices in use are deformable mirrors (DMs) and spatial light modulators (SLMs). DMs are reflective surfaces with an array of actuators that adjust the mirror shape, thereby altering the phase of reflected light. In an AO setup, the DM ideally reshapes the wavefront to have the inverse of the aberrations introduced by the optical system and scattering sample. SLMs, by contrast, are liquid-crystal-based devices that can modulate amplitude, phase, or polarization. DMs and SLMs remain the dominant approaches due to their availability and versatility (Figure 4A-C). Other actuation devices like electronically tunable lenses and digital mirror devices (DMDs) are less-frequently used for neuroimaging.

One configuration of DMs, the segmented DMs, consists of an array of discrete mirror segments (often arranged in a hexagonal or square grid), each mounted on actuators that provide piston (up/down) motion, and, sometimes, tip/tilt control. By adjusting each segment, the overall mirror approximates a piecewise planar correction of the wavefront. The advantage of segmented mirrors lies in their speed and high operational bandwidth. Since each actuator can be independently and parallelly driven, segmented DMs can achieve very high refresh rates on the order of 1–10 kHz or more (Yu et al. 2018). This makes them ideal for low-order, fast aberration corrections, such as compensating for rapid wavefront changes due to sample motion in closed-loop systems. An important limitation, however, is that the phase map they produce is discontinuous at the borders of segments due to the gaps between adjacent segments. Despite this, their speed and simplicity make them popular in applications by AO based on zonal aberration for cortical or retinal imaging (Rodríguez et al. 2021; Zhang et al. 2023b).

A more popular configuration, the continuous-faceplate DM, employs a single continuous reflective membrane or faceplate that is deformed by an array of actuators attached to its backside. The mirror surface bends smoothly, enabling fine and continuous phase variations across the aperture. Continuous DMs typically offer a larger number of actuators (hundreds to thousands) and can correct complex, high-order aberration patterns with high fidelity. This makes them particularly powerful for achieving near-diffraction-limited focusing through strongly distorted wavefronts, such as compensating for the many small phase errors introduced by deep cortical tissue). A trade-off, however, is that continuous DMs generally have slower response times than segmented designs, where typical devices operate at ~100 Hz, while high-performance models reach up to ~1 kHz (Rocha et al. 2024). The slower response arises partly from mechanical inertia and coupling within the membrane (motion in one actuator can influence neighboring regions as the mirror settles). Over-driving a continuous DM risks damage to the membrane or non-linear mechanical response. Continuous DMs have been successfully integrated into state-of-the-art three-photon microscopy systems with electrocardiogram gating for imaging at depths beyond 1.4 mm in the mouse brain, while maintaining near-diffraction-limited resolution, which enabled investigation of deep-layer layer-specific synaptic remodeling processes (Streich et al. 2021).

SLMs have comparatively slower response times, limited due to the relaxation characteristics. Yet, their pixelated electro-optical architecture offers exceptional versatility, providing thousands to millions of degrees of freedom for wavefront control. This architecture enables the generation of complex optical field distributions that can be precisely configured to match the geometric characteristics of neuronal structures or cortical vascular networks. Specifically, SLMs facilitate simultaneous formation of multiple diffraction-limited foci, the sculpting of elongated focal volumes, and the creation of specialized illumination patterns such as Bessel and Airy beams (Wang et al. 2014; Ayoub and Psaltis 2021). Such operational flexibility is especially valuable in functional neuroimaging applications requiring simultaneous interrogation of distributed neuronal ensembles or discrete vascular microdomains. However, these advantages are offset by inherent limitations, including reduced temporal update rates and constraints related to polarization sensitivity and wavelength dependence.

2.4.2. Sensing Strategies

While the actuators alone could, in theory, iterate through all possible patterns for the best image, such an approach is neither time-efficient nor conducive to high-throughput studies. Sensing aberrations at the sample plane is no small challenge because of several factors: a) while multiphoton microscopy has intrinsic depth-sectioning properties due to confinement of the focal spot, the wavefront sensors inherently do not receive the scattered signals from the focal plane alone, b) the biologically-relevant fluorescence signal levels from a single plane in the sample are too weak for reliable wavefront sensing, and c) the detected wavefront depends on the sample feature generating the fluorescence signals, which can vary drastically among tissue types and labels. Only the strategies that have been demonstrated for two-photon microscopy for deep-brain imaging are discussed here.

Two principal methodologies exist for wavefront sensing and correction: modal sensing, which employs a continuous surface wavefront corrector and represents the wavefront as a summation of discrete aberration modes (for example, Zernike polynomials); and zonal sensing, which models the wavefront as comprising discrete, non-overlapping spatial zones rather than continuous aberration modes distributed across the pupil aperture. Modal-based methodologies have been successfully implemented in (Débarre et al. 2009; Tang et al. 2012; Streich et al. 2021), and zonal-based approaches have been integrated into neuroimaging techniques in (Ji et al. 2010; Milkie et al. 2011; Rodríguez et al. 2021).

The principle of wavefront-sensing hardware is to measure the complex-valued magnitude and phase of the optical field. Thus, a simple camera cannot capture the wavefront; instead, the wavefront is often inferred through interference measurements or integrating measurements within sub-apertures. The most common device is the Shack–Hartmann WFS (SHWFS), which consists of a microlens array placed at the wavefront plane and a camera at the focal plane of the microlenses. When a local sub-aperture corresponding to a lenslet is tilted or aberrated, the focal spot shifts accordingly (Figure 4D). Similarly, pyramid WFS uses a four-faceted pyramidal prism at the focal plane to generate four distinct pupil images. Aberrations manifest as variations in the intensity distribution across these pupil images, thereby facilitating quantitative measurements of the aberrated wavefronts. In neuroscience, these methods have enabled two-photon morphological and functional imaging at depths of 700 μm (Wang et al. 2015) and recovery of diffraction-limited resolution across large cortical volumes (Qin et al. 2020).

In practice, biologically relevant fluorescence signals, such as from cells or sub-cellular structures in the brain, are often too dim for direct wavefront sensing. To overcome this, a reference signal is generated from within the tissue either by introducing contrast agents or labelling auxiliary structures in a complementary channel. This allows for independent measurement of the aberrated wavefront without repeated acquisition of the biologically relevant signals. There are generally two classes of guide stars in neural tissue:

Point-like guide stars: Like several concepts in AO borrowed from astronomy, ideal guide stars are perfect bright point emitters that generate the sharpest focal spots under ideal conditions. Unlike the sky, such features are not naturally present in all neural tissue. Instead, sub-diffraction fluorescent beads, injected microspheres, or labelled organelles such as boutons or synapses (e.g., quantum dots or fluorescently tagged vesicles) can serve as artificial point sources. Although they do not report neural activity, they provide stable references well suited for wavefront calibration.

Line-shaped guide stars: Because point-like sources are inherently weak emitters due to their small volume, randomly oriented thin fluorescent line emitters, such as blood capillaries, offer an alternative. By injecting fluorescent dyes (e.g., Cy5.5-dextran) into the bloodstream, capillary plasma emits bright, continuous fluorescence under two-photon excitation. These vascular structures act as extended fluorescent elements traversing multiple depths of tissue. When used as a wavefront reference, the optimization process leverages the their depth-spanning emission profiles to maximize signal sharpness or intensity, enabling correction of average aberrations across the corresponding imaging depth (Liu et al. 2019). Unlike other brain constituents that are line shaped like collagen or fiber bundles, capillaries span the entire depth range of imaging and are randomly oriented in any transverse plane. Therefore, they are ideal for any brain region and do not bias the aberration correction to certain directions.

Rather than estimating a deterministic wavefront from measured aberrations, the optimal DM pattern can be computed by optimizing an image-quality metric derived from acquired microscope images (Débarre et al. 2009), as described in Section 3.4.

2.4.3. Computational and hybrid strategies

The wavefront can be estimated deterministically if the detected sample field were complex-valued. For instance, in optical coherence microscopy (OCM), the availability of complex images allows sensorless estimation of aberrations and digital refocusing of all planes within a volume with a single acquisition (Adie et al. 2012). In a fluorescence microscope, the phase must be numerically reconstructed to achieve this. Phase-based computational approaches employ optical modeling and interference principles to determine or correct aberrations. A classic example is phase retrieval from intensity images is to acquire two or more images with known defocus offsets (or other phase diversity, such as one image in focus and another slightly out of focus), and computationally solve for both the object and the aberrated phase (Lee et al. 1997). Techniques of this kind, originally developed for astronomy, have been adapted to microscopy as “two-image” or “through-focus” aberration measurement approaches.

In multiphoton microscopy, methods such as the iterative multiphoton adaptive compensation technique (IMPACT) modulate half the elements of a MEMS at unique frequencies to create interference with the stationary elements over 2-5 iterations. This strategy enabled high-fidelity imaging of neuronal processes through the intact skull of mice (Tang et al. 2012). Another example of digital phase retrieval involves three-dimensional stacks and using neural field representations of the sample structure, which can then be inverted to retrieve the wavefront (Kang et al. 2024). A third approach integrates a coherence-gated wavefront sensor based on backscattered excitation light within a multiphoton microscope (Rueckel et al. 2006). This configuration was later expanded to a multimodal platform combining multiphoton microscopy and OCM within a single setup, where OCM served as digital WFS (Iyer et al. 2022).

Conventional sensorless AO techniques employ iterative deformable mirror adjustments guided by image-quality metrics. However, these metrics often exhibit inconsistent responses, fundamentally constraining the efficacy of aberration correction in biological tissues. Artificial intelligence and machine learning approaches have recently been introduced to address these challenges, showing promising results. The core idea is that an artificial neural network can learn to map distorted images directly to the required aberration corrections or to predict how to adjust a wavefront modulator to maximize image quality. This is appealing because it could significantly accelerate aberration corrections , handle low signal-to-noise conditions, and manage complex aberrations that traditional optimization fails to resolve.

One application is using deep neural networks (DNNs) to directly predict the wavefront distortions from the acquired images. For example, in single-molecule localization microscopy, researchers trained a DNN to process images of sparse, blinking fluorophores (which had aberrated PSFs) and output the corresponding Zernike coefficients of the aberration (Zhang et al. 2023a; Guo et al. 2025). A fundamental challenge in AI-based AO is acquiring suitable training datasets that serve as ground truth for supervised learning models. In supervised approaches, researchers can generate datasets by simulating unaberrated and aberrated PSFs, but such simulations often fail to capture the full heterogeneity of biological tissue. Alternatively, training datasets can be acquired experimentally by systematically introducing controlled aberrations through the actuators while recording the resulting images, thereby creating comprehensive aberration-to-image mapping datasets. Models trained in this manner can generalize effectively only when imaging conditions closely resemble those present during training.

Recent efforts have explored advanced learning paradigms, including unsupervised and physics-informed approaches that combine neural networks with optical modeling frameworks to enable partial self-calibration (Zhang et al. 2023b).

These systems can also integrate reinforcement learning elements by training networks during active experiments using objective functions such as image sharpness or contrast. Practical applications have shown strong performance, for example, Hu et al demonstrated a deep learning model for real-time two-photon imaging in the mouse brain (Hu et al. 2023). As in other fields of machine vision, the computational wavefront sensing problem is an ill-posed problem, making it well-suited for machine learning models that can exploit subtle image features undetectable by human-defined metrics. Additionally, the single-pass inference characteristic of these algorithms eliminates the need for iterative optimization and simplifies integration into closed-loop AO systems. To achieve practical adoption in brain imaging, future AI-based approaches should prioritize the creation of well-curated, biologically diverse training and validation datasets, reflecting realistic imaging conditions across samples, labels, and depths, rather than focusing solely on model architecture refinement.

3. METHODS

We present a step-by-step, tutorial-style guide to a 2P-AO with a DM utilizing a SHWFS and using the capillaries as guide stars, covering how to design, build, and evaluate an AO system, so that readers can more easily implement these techniques in their own laboratories.

3.1. Integrating adaptive optics components into existing multiphoton microscopes

Adaptive-optical multiphoton microscopy can be implemented in two ways: by building a system from the ground up or by retrofitting AO components into an existing microscope. Here we focus on the second: to effectively integrate AO into an established two-photon system. For this example, we will use a continuous DM in combination with a SHWFS. The same principles, however, apply to other choices of actuators and wavefront-sensing strategies. A typical multiphoton microscope consists of a laser output (1-2 mm), which is expanded to the aperture size of the first galvanometer scanning mirror (4-8 mm), translated to the second galvanometer mirror with a 1:1 magnification 4-f system, and then expanded to the back aperture of the objective lens (12-18 mm) using the scan and tube lenses. In an AO system, the DM and the WFS are placed between the laser output and the first scanner in a Fourier plane. This requires slight modifications to the beam paths, as discussed in the next sections.

3.1.1. Incorporate the DM into excitation beam path

The first consideration is to make full use of the DM's aperture. To achieve this, the laser beam must be expanded so that it fills the clear aperture of the DM. After reflection, the beam then needs to be reduced in size to match the aperture of the scanners. In practice, this is accomplished with a two-stage beam conditioning setup: one lens pair expands the beam to fully illuminate the DM, while a second lens pair shrinks it so that the scanners operate within their designed aperture.

The second consideration is the position of the DM within the optical train. In a pupil-plane AO configuration, the actuator should be conjugated to the back aperture of the objective. To meet this requirement, the lens pair between the DM and the scanners is arranged in a 4-f configuration. This setup re-images the DM onto the scanner plane, which in itself is conjugated to the objective pupil, ensuring that any phase corrections applied by the DM are faithfully projected to the back aperture.

Putting these elements together, the optical layout can be summarized as **Laser → Beam Expander (expand to DM) → DM → 4-f Relay Lenses (shrink and re-image) → Scanners → Scan Lens → Tube Lens → Objective (**Figure 5A). There are two considerations that will allow the reader to incorporate this into their existing scope easier, which are detailed in Notes 2-3.

3.1.2. Incorporating a descan pathway for direct wavefront sensing

The system described above is already capable of AO using sensorless wavefront sensing. To extend this approach and directly measure the distorted wavefront, the optical layout must be modified with a descanned wavefront sensing path. This pathway collects the emission from the guide star, descans it through the scanner system, and directs it onto a WFS for direct measurement. Conceptually, the descanned detection path can be summarized in Figure 5B. as: **Objective → Tube Lens → Scan Lens → Scanners → Dichroic → 4-f Relay → Short-pass Filter→ SHWFS (microlens array + EMCCD).** In this arrangement, the objective, tube lens, scan lens, and scanners are shared with the excitation path, so only the components downstream of the scanners need to be added to enable direct wavefront sensing.

The dichroic is introduced to separate the descanned emission light from the excitation optical path. Its cutoff wavelength should be chosen to lie between the excitation wavelength and the emission band, ensuring efficient reflection of the emission signal toward the WFS while transmitting the excitation beam. For example, with two-photon excitation at ~920 nm, a dichroic with a cutoff near 750–800 nm is typically used, so that the near-infrared excitation light passes through while the shorter-wavelength emission is reflected. To further protect the detection pathway, a short-pass filter with a similar cutoff should be placed in front of the WFS to block any residual excitation light. This step is important because the emission from the guidestar is a weak signal; therefore, the EMCCD used to detect it is highly sensitive. Even small amounts of leaked excitation beam can saturate or potentially damage the sensor.

The 4-f relay serves to conjugate the SHWFS to both the back aperture of the objective, ensuring that wavefront correction (via the actuator) and wavefront measurement are performed at the same conjugate location in the optical path. In addition, the 4-f relay also functions as a beam expander. See Notes 4-6 for details.

3.2. Calibration

The SHWFS measures aberrations as small shifts in the focal spots formed by its microlens array. The DM, in contrast, corrects these aberrations by adjusting the amplitudes of individual Zernike modes. To link the two systems, we need to know: *how much does each Zernike mode on the DM move the spots on the SHWFS?* This relationship is established through AO calibration. The goal of AO calibration is to build a calibration matrix that connects DM actuation (in terms of Zernike mode amplitudes) to SHWFS response (spot displacements). Once this matrix is known, it can be used to compute the DM correction pattern directly from SHWFS measurements.

Prepare the optical setup: Replace the objective with a mirror placed at the aperture plane. This allows the SHWFS to image the DM directly since the DM and SHWFS are conjugated to the back aperture of the objective.

Control the illumination: Insert a neutral-density (ND) filter with optical density ~3 into the laser path. This prevents excessive illumination on the SHWFS during calibration.

Record the reference pattern: Send a flatten command to the DM (no Zernike modes applied). The corresponding center locations of the $\boldsymbol{n}$ spots in the flat reference pattern can be represented as a $2\boldsymbol{n} \times 1$ vector $\mathbf{S_{Cref}}$, defined as

$$\mathbf{S_{Cref}} = \left(\underbrace{S_{\mathrm{Cref_1}} \cdots S_{\mathrm{Cref_n}}}_{\text{x-coordinates}},\ \underbrace{S_{\mathrm{Cref_{n+1}}} \cdots S_{\mathrm{Cref_{2n}}}}_{\text{y-coordinates}} \right)^T . \tag{5}$$

Record the Zernike modes pattern: Sequentially apply each Zernike mode to the DM with 1-μm root-mean-square amplitude and record the corresponding SHWFS spot. The center locations of the $\boldsymbol{n}$ spots for a given Zernike mode pattern i can be represented as a $2\boldsymbol{n} \times 1$ vector $\mathbf{S_{Cz_{\boldsymbol{i}}}}$, defined as

$$\boldsymbol{S}_{\boldsymbol{Cz}_i} = \left(\underbrace{S_{Cz_{i,1}} \cdots S_{Cz_{i,n}}}_{\text{x−coordinates}}, \underbrace{S_{Cz_{i,n+1}} \cdots S_{Cz_{i,2n}}}_{\text{y−coordinates}} \right)^T . \tag{6}$$

Compute spot displacements: For each Zernike mode, calculate the resulting SHWFS spot displacements relative to the reference pattern. The displacement vector for mode i, denoted $\mathbf{S}_{\mathbf{B}_i}$, is obtained by subtracting the reference pattern from the Zernike pattern:

$$\mathbf{S}_{\mathbf{B}_i} = \mathbf{S}_{\mathbf{Cz}_i} - \mathbf{S}_{\mathbf{Cref}} = \left(\underbrace{S_{\mathrm{Cz}_{i,1}} - S_{\mathrm{Cref}_1} \cdots S_{\mathrm{Cz}_{i,\mathrm{n}}} - S_{\mathrm{Cref}_\mathrm{n}}}_{\text{shifts on x}}, \underbrace{S_{\mathrm{Cz}_{i,\mathrm{n+1}}} - S_{\mathrm{Cref}_\mathrm{n+1}} \cdots S_{\mathrm{Cz}_{i,\mathrm{2n}}} - S_{\mathrm{Cref}_\mathrm{2n}}}_{\text{shifts on y}} \right)^T . \tag{7}$$

Construct the calibration matrix: Once all Zernike modes have been measured, combine the displacement vectors $\mathbf{S}_{\mathbf{B}_i}$ into a calibration matrix. Each column of this matrix corresponds to the SHWFS spot displacements induced by one Zernike mode with unit amplitude. Thus, the calibration matrix $\boldsymbol{Z2S}$ is a $2\boldsymbol{n} \times \boldsymbol{m}$ defined as

$$\boldsymbol{Z2S} = \left[\mathbf{S}_{\mathbf{B}_1} \, \mathbf{S}_{\mathbf{B}_2} \cdots \mathbf{S}_{\mathbf{B}_m} \right] , \tag{8}$$

where $\boldsymbol{m}$ is the number of Zernike modes included in the calibration. This matrix maps Zernike mode amplitudes to SHWFS spot deflections. Once $\mathbf{S}_\mathbf{B}$ is known, measured wavefronts from the SHWFS can be inverted through $\mathbf{S}_\mathbf{B}$ to compute the appropriate DM correction pattern. We describe the nuances to these procedures in Notes 7-8.

The next step is to correct for system aberration, which refers to imperfections in the microscope as well as aberrations introduced by the coverslip of the cranial window. Introducing a DM can also add system aberration, since more optical components are placed in the path and the DM itself may not be perfectly flat. However, the presence of the DM also provides a solution: it can be used to compensate for these aberrations. Because system aberrations do not vary with the sample, they can be corrected in advance as a calibration step. As long as the imaging system remains unchanged, this calibration does not need to be repeated. This step is critical, even if one intends to perform only indirect AO without direct wavefront sensing. The need for system correction calibration is detailed in Note 9.

1. Select the excitation wavelength: Perform calibration at the same wavelength you plan to use for imaging (for example, 920 nm for GCaMP). If direct wavefront sensing is used, also calibrate at the sensing wavelength (for example, 1,250 nm for Cy5.5 as a guide star).

2. Prepare the calibration sample: Make an aqueous fluorescent solution that can be excited at the chosen wavelength. We recommend fluorescein for 930 nm excitation, sulforhodamine B for 1,030 nm, and sulfo-Cy5.5 for 1,250 nm. Place the solution in a small chamber and seal it with a coverslip matching the thickness intended for the actual experiment. This ensures that the calibration reflects the true optical conditions of the imaging system. Check carefully for air bubbles, as they can distort the calibration results. Also, the details of preparing the solution are noted in Note 10.

3. Set up calibration imaging: Focus on the central 100 μm × 100 μm field of the fluorescent solution. Collect the emitted light with the PMT (or SiPM) in the same manner as conventional two-photon microscopy.

4. Optimize the intensity: The goal of the optimization is to maximize the average image intensity, I, by adjusting the amplitudes of the Zernike modes, displayed on the DM. Let

$$\mathbf{Z_{SyC}} = \left[Z_{\mathrm{SyC}_1}, Z_{\mathrm{SyC}_2}, \ldots, Z_{\mathrm{SyC}_\mathrm{m}}\right]^T \tag{9}$$

denote the Zernike coefficients applied to the DM, where each $Z_{Sy\mathrm{C}_j}$ represents the amplitude of the *j*-th Zernike mode. This is achieved with a gradient-descent algorithm for maximizing the image intensity. In each cycle, a small amplitude Δz_j of each Zernike mode is added one by one to the current DM pattern, and the change in mean intensity is measured. The gradient $\nabla_{\mathrm{Z_{SyC}}}\mathrm{I}$ with respect to each coefficient is then approximated as

$$\frac{\partial I}{\partial Z_{\mathrm{SyC}_j}} \approx \frac{I\left(Z_{\mathrm{SyC}_1}, Z_{\mathrm{SyC}_2}, \cdots, Z_{\mathrm{SyC}_j} + \Delta z_j, \cdots, Z_{\mathrm{SyC}_\mathrm{m}}\right) - I\left(Z_{\mathrm{SyC}_1}, Z_{\mathrm{SyC}_2}, \cdots, Z_{\mathrm{SyC}_j}, \cdots, Z_{\mathrm{SyC}_\mathrm{m}}\right)}{\Delta z_j}\,. \tag{10}$$

The Zernike coefficients are updated synchronously according to

$$Z_{\mathrm{SyC}_j}^{(t+1)} = Z_{\mathrm{SyC}_j}^{(t)} + \eta \frac{\frac{\partial I}{\partial Z_{\mathrm{SyC}_j}}}{\left\|\nabla_{\mathrm{Z_{SyC}}} I\right\|}\,, \tag{11}$$

where the gradient is normalized to preserve direction only, and η is the step size, typically chosen to correspond to an RMS amplitude of 10–20 nm. This process is repeated until convergence, which typically occurs after about 20-30 cycles, when the coefficients become stable. For this calibration, tip, tilt, and defocus should be excluded.

5. Collect the results and evaluate. The quality of the correction can be evaluated by imaging 200-nm fluorescent beads and measuring their PSF. After optimization, the PSF should approach the diffraction limit of the imaging system. Because the diffraction limit depends on both the excitation wavelength (λ) and the numerical aperture (NA) of the objective, the expected resolution will vary with different setups. As a rule of thumb, the theoretical full-width half maximum of the lateral resolution is approximately $0.5\,(\lambda/\mathrm{NA})$, and the axial resolution $(2\lambda/\mathrm{NA}^2)$. One can assess whether the system is performing near the diffraction limit by comparing the measured PSF with these theoretical values.

6. Collecting an aberration-free sample reference pattern: If direct wavefront sensing is planned, an additional step follows system aberration calibration. Apply the final system correction pattern $\mathbf{Z}_{\mathbf{SyC}}$ to the DM and then use the same aqueous solution of the guide-star dye (for example, sulfo-Cy5.5 conjugated to dextran) to record an aberration-free reference spot pattern on the SHWFS. This reference pattern will serve as the baseline for calculating sample-induced aberrations during *in vivo* imaging.

3.3. Guide-star-based adaptive optics

In our previous studies, we selected the ideal guide star using the guide in Note 11 based on the excitation-emission spectra, high quantum efficiency, and low toxicity. We chose the near-infrared dye, Cyanine 5.5 (Cy5.5) within the capillaries as the guide star, which has an emission peak in the near-infrared spectrum and a broad two-photon excitation spectrum with large cross-sections for over 200 nm (Figure 6). We delivered Cy5.5 to the mouse brain through retro-orbital injection into the bloodstream before each imaging session or alternatively, through tail-vein injection. Circulation in the bloodstream continuously refreshes the dye, which helps to prevent photobleaching of the dye. To ensure the dye does not leak out of the bloodstream into the surrounding tissue, Cy5.5 is conjugated to a 2-MDa dextran. With this conjugation, the guide star remains in the vessel lumen for more than 10 hours.

To correct for sample-induced aberrations, begin by identifying a microvessel, preferably a small capillary, within the field of view. Small capillaries typically yield more reliable correction than large arteries, which we suspect is because artery walls introduce aberrations confined to the lumen that do not generalize to the surrounding tissue. Visualize the vessel by imaging Cy5.5 (or another guide-star dye) in the lumen using conventional two-photon frame-scan imaging. At this stage, the guide-star emission is collected through the standard two-photon detection path and detected by the single photon detector. Once a suitable microvessel is identified, acquire the sample aberration pattern on the SHWFS using a long exposure. During this period, the excitation focus should scan across the vessel to obtain an average aberration pattern representative of the field of view. If the two-photon microscope has dual galvanometer mirrors, a line scan along the vessel can be used; otherwise, for galvanometer-resonant scanner systems, a frame scan is required. Adjust the exposure time, laser power, and EMCCD gain to optimize the signal, then save the recorded aberration pattern. The methods for the spatial extent of validity of the measured wavefront (isoplanatic patch) and optimizing the SNR of the measured wavefront are described in Notes 12 and 13.

After obtaining the wavefront-sensing pattern on the SHWFS, the next step is to analyze the pattern and solve the inverse problem to determine the correction to be applied on the DM. We denote by $\mathbf{S_S}$ the center locations of the $\boldsymbol{n}$ spots in the **sample aberration pattern**. This is represented as a $2\boldsymbol{n} \times 1$ vector:

$$\mathbf{S_s} = \left(\underbrace{S_{\mathrm{S}_1} \cdots S_{\mathrm{S}_\mathrm{n}}}_{\text{x-coordinates}}, \underbrace{S_{\mathrm{S}_{\mathrm{n}+1}} \cdots S_{\mathrm{S}_{2\mathrm{n}}}}_{\text{y-coordinates}} \right)^T . \tag{12}$$

The **aberration-free sample reference pattern**, recorded after system aberration calibration using an aqueous solution of the guide-star dye, is denoted as a $2\boldsymbol{n} \times 1$ vector:

$$\mathbf{S_{Sref}} = \left(\underbrace{S_{\mathrm{Sref}_1} \cdots S_{\mathrm{Sref}_\mathrm{n}}}_{\text{x-coordinates}}, \underbrace{S_{\mathrm{Sref}_{\mathrm{n}+1}} \cdots S_{\mathrm{Sref}_{2\mathrm{n}}}}_{\text{y-coordinates}} \right)^T . \tag{13}$$

The **spot-shift array**, representing the sample-induced aberration, is then obtained as the difference between the two patterns:

$$\mathbf{\Delta S_S} = \mathbf{S_S} - \mathbf{S_{Sref}} = \left(\underbrace{S_{\mathrm{S}_1} - S_{\mathrm{Sref}_1} \cdots S_{\mathrm{S}_\mathrm{n}} - S_{\mathrm{Sref}_\mathrm{n}}}_{\text{shifts on x}}, \underbrace{S_{\mathrm{S}_{\mathrm{n}+1}} - S_{\mathrm{Sref}_{\mathrm{n}+1}} \cdots S_{\mathrm{S}_\mathrm{n}} - S_{\mathrm{Sref}_{2\mathrm{n}}}}_{\text{shifts on y}} \right)^T . \tag{14}$$

To translate the spot-shift array into Zernike mode amplitudes, we project $\mathbf{\Delta S_S}$ onto the calibration basis $[\mathbf{S_{B_1}}, \mathbf{S_{B_2}}, \dots, \mathbf{S_{B_{\mathit{m}}}}]$ which was obtained previously by AO calibration. This yields the Zernike coefficient vector $\mathbf{Z_{Spl}}$:

$$\mathbf{Z_{Spl}} = \boldsymbol{Z2S}^{+}\mathbf{\Delta S_S}, \tag{15}$$

where $(\cdot)^+$ denotes the generalized matrix inverse. Therefore, the DM pattern for correcting the sample aberration in terms of Zernike modes, denoted, $\mathbf{Z_{SplC}}$, is obtained as

$$\mathbf{Z}_{\mathbf{SplC}} = -\mathbf{Z}_{\mathbf{Spl}}. \tag{16}$$

When combined with the system aberration correction, the final DM command in Zernike space, $\mathbf{Z}$, is given by

$$\mathbf{Z} = \mathbf{Z}_{\mathbf{SplC}} + \boldsymbol{Z}_{\mathbf{SyC}}. \tag{17}$$

Finally, the corresponding command voltages for the individual DM actuators, denoted $\mathbf{C}$, are obtained through the Zernike-to-Command matrix ($\boldsymbol{Z2C}$)

$$\mathbf{C} = \boldsymbol{Z2C}\,\mathbf{Z}\,. \tag{18}$$

After applying this pattern to the DM, the excitation wavelength can be switched to that of the intended fluorophore (e.g., 920 nm for GCaMP), and imaging proceeds as in conventional two-photon microscopy.

3.4. Image-based aberration correction

Often, having a dedicated WFS is not feasible, especially in multichannel imaging applications where having a dedicated channel for guide stars is not available. While a few researchers have utilized the scattered light or a separate monochromatic laser for wavefront sensing in ophthalmology, the scattering from the superficial layers in the brain dominate the detected wavefront signals, hereby creating a bias. Thus, sensorless methods for wavefront engineering are a popular alternative. Broadly, there are two kinds of techniques used to achieve this: image-based optimization of the wavefront and phase or PSF retrieval. While some techniques among the latter are purely computational, where the images are corrected rather than the incident wavefronts, the methods are nonetheless a useful set of tools for digital wavefront sensing.

The first and the most critical step in image-based optimization is the choice of the objective function, which must be computed quickly and must avoid biases within the image. For instance, while image intensity is an obvious choice, often, the algorithm could bias the correction towards brighter features from other, often superficial, planes in the sample than the plane of interest. Similarly, optimizing the high-frequency components agnostically could also yield in highly astigmatic beams aligned along neuronal fiber tracts or capillary features, rather than holistic optimization. The metrics are discussed in detail in the next section. A combination of these metrics with different weights can offer better optimization for general brain imaging, and the objective function could be tuned for best performance based on the sample and the label. For instance, the objective function for imaging neurotransmitter signals from spines/ boutons optimizing for point-like micrometer-scale structures may not be same function for capturing the Calcium dynamics from the soma.

Second, the optimization algorithm plays a crucial role in the convergence and effectiveness of the solution, where stochastic multivariate methods have best performance, practically. Apart from standard optimization techniques, there is an increasing trend of using machine learning models to estimate the wavefront or optimal deformable mirror pattern for a given image, as described in Section 2.4.3. While adaptability of machine learning models from one instrument to another remains a main challenge for generalized utility, the fully computational nature of these algorithms without the need for multiple image acquisitions make it an attractive area for sensorless AO.

Third, real-time implementation of image-based aberration correction enables a completely closed-loop solution, accounting for any dynamics in aberrations over the course of experimentation. While acquiring a hundred image frames will only need a few seconds of acquisition in modern multiphoton microscopy setups, the bottleneck is often in computing the objective functions. Making these computations on a graphics card can help overcome these challenges. Real-time computation of these functions will also help evaluate the effectiveness of AO in practical conditions, as described in the next section.

3.5 Evaluation

Metrics for evaluating AO performance can be broadly divided into **image-based metrics**, which capture optical quality in terms of intensity, contrast, sharpness, or frequency content, and **biological or functional metrics**, which quantify improvements in the visibility or fidelity of biologically meaningful structures. The choice of metric depends strongly on the microscope modality: a metric that performs well for multiphoton imaging may be unsuitable for widefield microscopy (Hampson et al. 2021).

3.5.1. Image-based quality metrics

These metrics are based on the image itself and do not directly depend on the biological process being measured. They describe how clear, bright, and sharp an image appears after aberration correction. Image-quality metrics are typically divided into two categories: a) spatial-domain metrics, calculated directly from pixel values (e.g., brightness, sharpness, contrast); and b) frequency-domain metrics, derived from the Fourier transform of the image to assess how much detail is preserved at different spatial frequencies.

The simplest and most direct metric is **total image intensity**, defined as the sum of all pixel values within the image,

$$\mathrm{I}_{\mathrm{total}} = \sum \mathrm{I}(x, y)\,. \tag{19}$$

In multiphoton microscopy, the focal fluorescence emission scales with the square (2P) or cube (3P) of the focal intensity. The signal loss from aberrations is much more obvious than scattering-based systems. Consequently, AO correction frequently produces large intensity gains, ranging from ~2× to over 30×, depending on imaging depth and feature size (Wang et al. 2015; Qin et al. 2020; Rodríguez et al. 2021; Streich et al. 2021). For example, in hippocampal CA1 neurons imaged with two-photon endomicroscopy, AO increased signal intensity up to ~6×, enabling synaptic resolution at 300 μm depth (Wang et al. 2015; Qin et al. 2020). In zebrafish myotomes, AO correction yielded 1.2–5× increases in two-photon fluorescence intensity, while in mouse cortex, YFP-labelled dendrites at 370–500 μm below the dura exhibited intensity enhancements of ~2.7× (Rodríguez et al. 2021). Three-photon imaging at 760 μm depth has shown dendritic signal gains of 8–30×, with the strongest improvements observed for the finer structures (Rodríguez et al. 2021). In intravital three-photon microscopy of mouse cortex, up to eight-fold in signal intensity were reported, confirming AO's role in restoring axial resolution (Streich et al. 2021). A repeatable ≥ 2× increase in total or mean intensity is generally accepted as evidence of successful AO correction (Facomprez et al. 2012).

For sparse structures such as dendritic spines, the **metric** y_{m}, calculated from only the brightest pixels, offers greater robustness to background fluctuations and provides a more reliable measure of intensity in non-linear imaging systems (Hu et al. 2023). It is defined as:

$$\mathrm{y}_{\mathrm{m}} = \sum_{\mathrm{i}}^{\mathrm{m}} \mathrm{T}(\mathrm{i})\ , \tag{20}$$

where pixel intensities are arranged in descending order as $\mathrm{T(i)}$, and only the top m values are summed (Hu et al. 2023). While brightness-based metrics are straightforward and powerful, they are not universally applicable. Contrast-based metrics, such as the root mean square (RMS) contrast, provide additional information about image structure and feature visibility.

$$RMS = \sqrt{\frac{1}{N}\sum (\mathrm{I}(x, y) - \langle I \rangle)^2}\,, \tag{21}$$

where $\langle I \rangle$ is the mean intensity over the region of interest. When AO correction sharpens fine features, the disparity between bright and dark regions increases, resulting in 2–12× gains in RMS contrast, enabling clear visualization of dendritic spines and other structures up to 500 μm deep in zebrafish myotomes and mouse cortex (Rodríguez et al. 2021).

Often, signal increases are accompanied by changes in image background levels. To account for this, several derived contrast metrics are used, including signal-to-noise ratio (SNR), signal-to-background ratio (SBR), contrast-to-noise ratio (CNR), and peak-to-background ratio (PBR). Given the mean signal intensity, $\langle I \rangle$, mean background intensity, $\langle B \rangle$, and standard deviation of background, σ_B,

$$SNR = \frac{\langle I \rangle}{\sigma_B}\,, \tag{22}$$

$$SBR = \frac{\langle I \rangle}{\langle B \rangle}\,, \tag{23}$$

$$CNR = \frac{\langle I \rangle - \langle B \rangle}{\sigma_B}\,, and \tag{24}$$

$$PBR = \frac{T(0)}{\langle B \rangle}\,. \tag{25}$$

These measures provide complementary insights: SBR reflects relative brightness, whereas CNR accounts for noise fluctuations. In deep three-photon imaging of mouse cortex and subcortical white matter, AO correction has been shown to increase SBR several-fold, revealing dendrites, spines, and microvasculature otherwise indistinguishable (Streich et al. 2021). In sensorless AO implementations, SBR is often used directly as the optimization metric for shaping the deformable mirror (DM) (Liu et al. 2019).

Fourier-based analysis provides another perspective by quantifying resolution recovery, examining how aberrations suppress high spatial frequencies. As discussed in Section 2.1, the fine structural details in the space domain correspond to high-frequency content in *k*-space. For instance, the High Frequency Fourier Metric (HFFM) integrates the signal power within mid-range frequencies (0.1 to 0.6 of maximum k-space frequency, f_{max}), reflecting PSF sharpness while minimizing contributions from low-frequency specimen structure (low-k) or high-frequency noise (high-k),

$$HFFM = \int_{0.1\,f_{max}}^{0.6\,f_{max}} \left|\hat{I}(k)\right|^2 dk\,,. \tag{25}$$

The Threshold Metric measures the resolved bandwidth by identifying, in each angle in Fourier space, the farthest spatial frequency whose power exceeds a defined noise threshold. Averaging these maxima across all directions yields an estimate of the practical resolution limit, the extent to which AO recovers high-frequency information despite specimen- or system-induced noise. This metric is particularly valuable in widefield and 3D structured illumination microscopy (3D SIM), where it links AO performance directly to usable bandwidth.

$$\mathrm{y_T} = \frac{\int_0^{2\pi} \hat{I}_T(\theta) d\theta}{\int_0^{2\pi} d\theta}. \tag{26}$$

For each angular direction in Fourier space, the maximum spatial frequency $\hat{I}_T(\theta)$ that exceeds a predefined noise threshold T is identified. Finally, the Fourier Ring Correlation (FRC) metric objectively estimates resolution in super-resolution by comparing reproducibility of spatial frequencies in independently acquired images. The resolution limit is defined as the spatial frequency where the FRC curve falls below a set threshold (typically 0.143), making it the gold standard method for super-resolution nanoscopy and digital AO:

$$FRC(q) = \frac{\sum_{i \in ring(f)} F_1(i) F_2^*(i)}{\sqrt{\sum |F_1(i)^2| \sum |F_2(i)^2|}} \tag{27}$$

Figure 7 illustrates several of these metrics, evaluated from an image acquired from somatostatin-expressing Layer 5b neurons of the mouse somatosensory cortex, acquired using the setup described in (Yao et al. 2023) imaged between 670-690 µm. Visually, one can observe the higher intensity and appearance of finer structures after full AO correction (compared to system AO only) in Figure 7a. The examples of the cross section show how new dendritic structures become apparent and resolvable from one another after correction (Figure 7b). In the Fourier space, more signal is distributed within the higher spatial frequencies (above between 2 and 1 µm^{-1}, corresponding to the features between 0.5-1 µm, Figure 7c). The intensity metrics $\mathbf{y_m}$ and RMS contrast show small but statistically significant increases (Figure 7d-e). The distributions of the SNR, SBR, PBR, or CNR are dependent on the choice of the chosen background, which can vary between different depths (Figure 7f-i). Nonetheless, there is an increase of 1.25-2.5x in these metrics after correction. These can be analyzed in the distribution of the intensities, where there is a decrease to the image background (at 3000-4000 arbitrary intensity units), an increase to the weak signals up to 15,000 a.u., and an increase to the brightest features beyond 20,000 a.u. (Figure 7j). In the k-space, there is a corresponding increase to the intensity at higher spatial frequencies (0.5-4 µm^{-1}) (Figure 7k). Quantitatively, this is apparent in the 1.5x increase to the HFFM (Figure 7l).

While no single metric can fully capture image quality in AO combining multiple complementary metrics provides a more complete evaluation of performance. While these metrics are largely sample agnostic, there are a few metrics that more closely describe the biologically relevant significance of AO, described in the next section. In practice, they provide some of the most compelling demonstrations of the capability of AO, since they directly link optical correction to improved biological insight.

3.5.2. Sample-induced metrics

Unlike the previous metrics, the measures discussed here require additional pre-processing, including manual or semi-automated selection of cell bodies, boutons, spines, or dendrites within the field of view. A widely used biological metric is the fractional change in fluorescence ($\Delta F/F_0$), the standard readout in calcium, glutamate, or voltage imaging. AO correction reduces the temporal noise floor and enhances $\Delta F/F_0$, thereby enabling reliable detection of neuronal activity.

In hippocampal imaging of awake mice, AO allowed tightly packed neurons to be clearly separated, permitting accurate recording of calcium transients without interference from neighboring cells and with reduced neuropil contamination (Qin et al. 2020). AO correction improves $\Delta F/F_0$ by lowering temporal noise and minimizing crosstalk between adjacent neurons. In hippocampal CA1 pyramidal neurons of Thy1-GFP mice, AO enabled clear separation of tightly packed neurons, yielding accurate calcium-transient recordings that were previously confounded by background fluorescence (Rodríguez et al. 2021). In the mouse spinal cord dorsal horn, AO facilitated recording of somatosensory-evoked calcium transients at depths exceeding 300 μm, where conventional imaging fails. Under these conditions, signal intensity improved 5.9-fold, and $\Delta F/F_0$ amplitudes increased 2.1-fold (Rodríguez et al. 2021).

Similarly, another powerful biological metric is the apparent width or resolvability of subcellular structures such as dendritic spines, axonal boutons, capillaries, or immune cells. In hippocampal CA1 neurons imaged with two-photon endomicroscopy, AO combined with deconvolution reduced the FWHM of spine cross-sections to as low as 0.45 μm, while simultaneously increasing fluorescence intensity to reveal spines at depths up to 300 μm (Rodríguez et al. 2021). In cortical imaging, AO enabled visualization of dendritic spines and axonal boutons that were previously invisible in uncorrected images.

In vivo three-photon microscopy further extended these improvements, resolving synaptic structures as deep as 870 μm below the dura and enabling clear imaging through highly scattering white matter (Rodríguez et al. 2021). The same principles apply in even more challenging tissues. In the mouse spinal cord, where high neuronal density and surface curvature typically restrict two-photon imaging to shallower depths (<200 µm), AO-assisted three-photon microscopy revealed fine neuronal morphologies beyond 400 µm, with fluorescence signals improving by up to 7-fold (Rodríguez et al. 2021). In the mouse cortex, near-diffraction-limited resolution was preserved at depths exceeding 1.4 mm, enabling individual synapses to be resolved (Streich et al. 2021).

4. CONCLUSIONS

We have outlined the fundamental challenges and enabling solutions for high-resolution imaging of neural and vascular dynamics in the mouse cortex using wavefront engineering. The complexity of brain tissue, with its heterogeneity and layered structure, imposes severe optical aberrations that degrade both image resolution and signal strength, particularly at increasing imaging depths. Conventional two-photon microscopy, while transformative, remains fundamentally constrained by sample-induced aberrations, limiting reliable subcellular imaging to superficial cortical layers. Adaptive optics techniques, leveraging deformable mirrors, spatial light modulators, and advanced wavefront-sensing strategies directly mitigate these effects by correcting aberrations in real time, thereby extending the reach of high-resolution imaging across the entire cortical column. Complementary approaches, such as beam multiplexing, guide-star strategies, computational or artificial-intelligence-based methods are rapidly pushing the technical frontier, making previously inaccessible neural and vascular dynamics observable at millisecond and micrometer scales.

Crucially, the effectiveness of these corrections is best captured not by a single parameter, but by an ensemble of quantitative metrics, encompassing image intensity, contrast, sharpness, frequency content, and biological relevance. Metrics such as total intensity, SNR/SBR, and frequency-domain analyses each yield distinct yet complementary insights into system performance. The selection of appropriate metrics should be guided by both experimental objectives and sample characteristics, as no single measure can comprehensively describe image quality across all imaging contexts. When reading this chapter, readers should remember that successful wavefront engineering requires both mastery of the underlying optical physics- the mechanisms of aberration formation and correction, and rigorous evaluation of biological performance in meaningful physiological terms. As the field continues to evolve rapidly, maintaining a modular and integrative perspective—combining multiple correction and evaluation strategies—will be essential for driving new discoveries in neural circuit dynamics and microvascular physiology.

NOTES

1. Orthogonality of Zernike polynomials

While Zernike polynomials are theoretically orthogonal, the discrete nature of the deformable mirror imparted on a continuous membrane, the hysteresis of the mirror pistons, and precision of deformations cause several local minima. Thus, a standard hill-climbing algorithm for each aberration will cause convergence to local minimum. In a multivariate optimization algorithm for all aberrations at once, optimizing for higher-order aberrations increases the parameters for optimization for the same metrics. A stochastic multivariate method with adaptive weights is a balance between the two methods with the fastest convergence to the global minimum.

2. Beam separation at the deformable mirror

The DM is a reflective device designed to operate optimally with a near-normal incident beam (0° angle). A common way to separate the incoming and reflected beams is to use a polarizing beam splitter (PBS) in combination with a quarter-wave plate. However, because the beam is expanded to fill the DM (e.g., ~15 mm diameter), this would require a large PBS, which can introduce significant dispersion and reduce two-photon excitation efficiency. To avoid this issue, we recommend introducing a small incident angle (typically <5°) on the DM. This approach provides efficient beam separation without relying on large, dispersive PBS.

3. Fine tuning of the 4-f configuration for DM

The 4-f relay (**DM → Lens 1 → Lens 2 → Scanner**) must be carefully tuned to ensure proper conjugation of the DM to the scanner plane. This requires flexibility in adjusting both the separation of the relay lenses and the position of the DM relative to the relay. For this reason, these optical elements should ideally be mounted on translational stages or a rail system, allowing precise adjustments without disturbing the overall alignment. Practical conjugation procedure is as follows**:**

- Remove **Lens 1** and move **Lens 2** along the optical axis until it focuses onto the scanner.
- Replace **Lens 1** and adjust its position along the optical axis until the output beam is collimated.
- Replace the **objective** with a camera whose sensor is positioned at the back-aperture plane of the objective. A correct conjugation should re-image the DM onto this plane.
- Temporarily replace the **DM** with a scratched mirror (since the DM surface itself lacks visible features).

- Translate the scratched mirror along the optical axis until the scratch appears sharply imaged on the camera sensor—this defines the conjugate plane.
- Finally, replace the scratched mirror with the **DM**.

4. Descanned beam expansion and trade-offs

Expanding the beam onto the microlens array increases the number of illuminated lenslets, which improves the precision of wavefront estimation and enables correction of higher-order Zernike modes. However, distributing the light across more lenslets reduces the intensity per spot and thereby lowers the signal-to-noise ratio (SNR) for wavefront sensing. The number of Zernike modes that can be corrected is fundamentally limited by the number of slope measurements available: correcting up to radial order $\boldsymbol{n_r}$ requires $(\boldsymbol{n_r}+1)(\boldsymbol{n_r}+2)/2$ modes, and thus at least half as many lenslets, $(\boldsymbol{n_r}+1)(\boldsymbol{n_r}+2)/4$, since each lenslet provides two independent measurements (x and y slopes). In practice, however, stable and accurate correction typically requires a higher sampling density. As a rule of thumb, on the order of $(\boldsymbol{n_r}+1)^2$ illuminated lenslets could reliably reconstruct modes up to order $\boldsymbol{n_r}$.

In practical terms, a good starting point is to size the beam such that the number of illuminated lenslets, $\boldsymbol{n}$, approximately matches the number of actuators on the deformable mirror (DM), thereby balancing the resolution of measurement and correction. If the signal-to-noise ratio becomes limiting, the beam can be reduced to concentrate more light per lenslet, with the tradeoff that the maximum correctable Zernike order decreases. This balance between resolution and measurement sensitivity defines the effective operating range of a Shack–Hartmann–based AO system.

5. Fine tuning of the 4-f configuration for SHWFS

Similar to the DM, the 4-f relay for the SHWFS (**Scanner → Lens 3 → Lens 4 → Microlens Array → EMCCD**) must be carefully tuned to ensure proper conjugation of the WFS to the back aperture of the objective. The related optical elements should ideally be mounted on translational stages or a rail system. Follow these steps for a practical guide:

- Place a **guide-star aqueous solution** at the sample plane. Excite it and use its emission as the light source for the following alignment steps.
- Adjust **Lens 3** along the optical axis so that the scanner is positioned at its focal plane. Since Lens 3 is located after the scanner, this step is typically performed using mechanical measurements (e.g., with a caliper) to set the distance accurately.

- Adjust **Lens 4** along the optical axis to collimate the emission beam. Collimation can be verified by temporarily removing the microlens array and translating the EMCCD along the optical axis—if the beam size remains constant on the detector, the beam is collimated.
- Remove **Lens 3** and translate the **EMCCD** along the optical axis until the emission light is focused on the detector. The detector plane now defines the conjugate plane. Conjugation can be verified by replacing the objective and sample with a paper target placed at the back-aperture plane of the objective; when illuminated with a flashlight, a clear image of the target should form on the EMCCD.
- Replace **Lens 3** and the **microlens array**. Move the microlens array along the optical axis until the emission spots are best focused on the detector.
- Translate the **microlens array together with the EMCCD** along the optical axis so that the microlens array sits precisely at the conjugate plane.

6. Where does the Shack-Hartmann wavefront sensor go into the system?

The SHWFS approximates the local slope of the wavefront by tracking the corresponding displacement of each part of the wavefront corresponding to a lenslet. There are two possible locations for the Shack-Hartmann sensor. If one follows the logic in Figure 2B, the lenslet array is placed at a distance equivalent to the focal length from the Fourier plane 3 in Figure 5B, such that the displacement is linearly proportional to the slope. However, the part of the wavefront corresponding to each lenslet has overlap with adjacent ones since the aperture is not at the Fourier plane, but at the same plane as the lenslet array. Thus, the more common practice is to place the lenslet array directly at the Fourier plane and deal with the deviations from the Fourier transform pairs through calibration. While most practical WFS use lenslet arrays with small focal lengths (~5 mm) rendering these the difference between the two locations largely insignificant, recent custom WFS utilize lenslet arrays with larger focal lengths (Wang et al. 2015; Yao et al. 2023) where this difference cannot be ignored. The larger quantitative analysis between these locations will be discussed in a future publication.

7. Mirror alignment for AO calibration

Place the mirror at the back aperture of the objective. The key here is the angle: you want the reflected beam to travel along the optical axis of the descanned path. A simple way to do this is to mount the mirror on a kinematic mount. Next, remove the microlens array in front of the EMCCD, and then adjust the mirror angle until the reflected beam stays fixed in place as you move the EMCCD along the optical axis.

8. DM calibration

The DM is typically controlled by specifying the RMS amplitudes of Zernike modes, but the device itself operates through voltages applied to individual actuators. To link these representations, the manufacturer provides a precalibrated **Zernike-to-Command (*Z2C*) matrix**, which converts Zernike amplitudes into actuator voltages.

The factory calibration includes command sets for producing a flat mirror and for driving each of Noll's Zernike modes at 1 µm RMS amplitude. These define the mapping:

$$\boldsymbol{Z2C} = [\mathbf{c_1}\ \mathbf{c_2} \ldots \mathbf{c_m}] \tag{28}$$

where each $\mathbf{c_i}$ is a vector of actuator voltages that generates the i-th Zernike mode at 1 µm RMS amplitude. If this calibration drifts and the DM no longer reproduces the intended modes, the instrument should be returned to the manufacturer for recalibration.

9. Why indirect AO should also include system aberration calibration

System aberrations can, in principle, be corrected through iterative optimization during indirect (sensorless) AO. However, this requires extra optimization cycles and makes the indirect method slower. System aberrations and sample-induced aberrations need to be separated when demonstrating performance. To properly show the benefit of an indirect AO method, results should always be compared against imaging where system aberrations have already been calibrated and corrected. If the comparison is made against completely uncorrected imaging (no AO at all), the apparent improvement may simply reflect the correction of system aberrations introduced by the optics, rather than the correction of aberrations caused by the sample.

10. What is the concentration for the aqueous fluorescent solution

If the concentration is too low, the signal-to-noise ratio may be insufficient to reliably estimate the gradient. Although increasing the laser power can compensate for this noise, it risks saturating the fluorophores. Once saturation occurs, the optimization may incorrectly try to enlarge the PSF rather than confine it, in order to excite more fluorophores. If the concentration is too high, the emitted light can be reabsorbed by the solution itself, causing the optimization to falsely shift the PSF upward to reduce absorption.

As a general guideline, use low laser power (<5 mW) to avoid fluorophore saturation. The dye concentration should then be verified by examining the histogram of the image intensity. Ideally, the histogram should span a reasonable portion of the detector's dynamic range. If it only occupies a narrow range, the gradient signal may be too noisy for the optimization to converge, and the concentration should be increased. Finally, check the histogram while moving the focus along the z-axis. It should remain stable and not shift with depth; if shifts are observed, the dye concentration should be diluted until the histogram is consistent.

11. Guide-star selection considerations

There are several important factors to consider when choosing a guide star. The first is the **emission spectrum**. Because the guide star's emission is used to estimate the aberrations experienced by the excitation beam, its emission wavelength should ideally be close to the excitation wavelength of the fluorophore used for imaging. The closer these match, the more accurately the measured aberrations reflect the true imaging conditions. The second is the **quantum efficiency** of the dye, which needs to be sufficiently high for detection by a WFS with lower sensitivity than single-photon detectors. In this setup, the emission is collected by an EMCCD rather than a PMT or SiPM. This means we require not only sufficient overall brightness, but also a clean spatial spot pattern formed by the microlens array. A dye with high quantum efficiency ensures that enough photons are captured to generate sharp, reliable spot images. Third, because the dye is delivered *in vivo via* intravenous injection, low toxicity is essential to minimize harm to the animal. Other practical factors, such as water solubility and cost, should also be considered.

In practice, trade-offs are often necessary. For example, we use **Cyanine5.5** as the guide star dye. This near-infrared dye has an emission peak at 695 nm, which is not especially close to the 920 nm excitation wavelength commonly used for GFP imaging, but it represents a practical balance among emission wavelength, brightness, water solubility, cost, and toxicity.

Finally, it is worth noting that one of the main bottlenecks for the imaging depth of adaptive-optical two-photon microscopy is the depth limit of direct wavefront sensing. This limit is set primarily by the strength of the guide star signal, which becomes weaker with depth because scattering and absorption increase as the emission travels through tissue. A practical way to overcome this challenge is to develop or identify brighter dyes with longer emission wavelengths. Longer wavelengths scatter and absorb less in tissue, allowing photons to propagate from deeper layers with reduced loss. As a result, both the sensing depth and the overall imaging depth can be significantly extended.

12. Isoplanatic patch

Sample aberrations are not uniform across the brain; they change from region to region. This means that each field of view needs its own correction during an experiment. The area over which one correction still improves image quality is called the **isoplanatic patch**. In the mouse brain, this patch is only a few hundred micrometers across. In practice, it works well to correct aberrations for every 100 μm×100 μm field of view—or even smaller, such as 50μm×50μm. A single correction pattern can usually be applied within an axial depth range of about ±50 μm.

13. Optimizing the SNR for wavefront sensing

As discussed above, the depth limitation of wavefront sensing is one of the main bottlenecks in two-photon microscopy with direct AO. Beyond a certain depth, the wavefront-sensing pattern recorded by the SHWFS often degrades until the signal-to-noise ratio (SNR) is too low to extract a reliable aberration map, preventing effective correction. Achieving a wavefront-sensing pattern with sufficient SNR is therefore essential. Several strategies can help improve SNR:

Increase laser power: Raising excitation power can markedly improve SNR, but excessive power risks photodamage in brain tissue. We recommend keeping the power under the objective below ~200 mW.

Increase exposure time: Longer exposures also enhance SNR, but excessive exposure can accumulate heat and damage tissue, especially at depth where power is already high. Setting exposure times in the range of 0.5–30 s helps balance SNR gain against heating.

Optimize scanning strategy: If possible, use line scans along a vessel during wavefront sensing so that the excitation beam spends most of its time generating signal. Frame scanning is less efficient, as much of the scan passes outside the guide star, producing little signal but still adding heat.

Adjust EMCCD gain: Increasing EM gain reduces read noise and therefore improves the SNR, but it also amplifies shot noise and therefore does not improve the signal-to-shot-noise ratio. For this reason, EM gain should be adjusted only after optimizing laser power and exposure time.

REFERENCES

Adesnik H, Abdeladim L (2021) Probing neural codes with two-photon holographic optogenetics. Nat Neurosci 24:1356–1366. https://doi.org/10.1038/s41593-021-00902-9

Adie SG, Graf BW, Ahmad A, et al (2012) Computational adaptive optics for broadband optical interferometric tomography of biological tissue. Proc Natl Acad Sci USA 109:7175–7180. https://doi.org/10.1073/pnas.1121193109

Aggarwal A, Liu R, Chen Y, et al (2023) Glutamate indicators with improved activation kinetics and localization for imaging synaptic transmission. Nat Methods 20:925–934. https://doi.org/10.1038/s41592-023-01863-6

Ayoub AB, Psaltis D (2021) High speed, complex wavefront shaping using the digital micro-mirror device. Sci Rep 11:18837. https://doi.org/10.1038/s41598-021-98430-w

Beaulieu DR, Davison IG, Kılıç K, et al (2020) Simultaneous multiplane imaging with reverberation two-photon microscopy. Nat Methods 17:283–286. https://doi.org/10.1038/s41592-019-0728-9

Chen T-W, Li N, Daie K, Svoboda K (2017) A map of anticipatory activity in mouse motor cortex. Neuron 94:866-879.e4. https://doi.org/10.1016/j.neuron.2017.05.005

Chen T-W, Wardill TJ, Sun Y, et al (2013) Ultrasensitive fluorescent proteins for imaging neuronal activity. Nature 499:295–300. https://doi.org/10.1038/nature12354

Clairaut A-C (1762) Mémoire sur les moyens de perfectionner les lunettes d’approche: par l: usage d’objectifs composés de plusieurs matieres differemment réfringentes. De l’Imprimerie Royale

Conrady AE (1918) The five aberrations of lens-systems. Monthly Notices of the Royal Astronomical Society 79:60. https://doi.org/10.1093/mnras/79.1.60

Dalangin R, Jia BZ, Qi Y, et al (2025) Far-red fluorescent genetically encoded calcium ion indicators. Nat Commun 16:3318. https://doi.org/10.1038/s41467-025-58485-z

Débarre D, Botcherby EJ, Watanabe T, et al (2009) Image-based adaptive optics for two-photon microscopy. Opt Lett 34:2495–2497. https://doi.org/10.1364/ol.34.002495

Deng F, Wan J, Li G, et al (2024) Improved green and red GRAB sensors for monitoring spatiotemporal serotonin release *in vivo*. Nat Methods 21:692–702. https://doi.org/10.1038/s41592-024-02188-8

Drobizhev M, Molina RS, Hughes TE (2020) Characterizing the Two-photon Absorption Properties of Fluorescent Molecules in the 680-1300 nm Spectral Range. Bio Protoc 10:e3498. https://doi.org/10.21769/BioProtoc.3498

Duffieux PM (1983) The Fourier transform and its applications to optics, 2nd ed. Wiley, New York

Ebrahimi S, Lecoq J, Rumyantsev O, et al (2022) Emergent reliability in sensory cortical coding and inter-area communication. Nature 605:713–721. https://doi.org/10.1038/s41586-022-04724-y

Emiliani V, Entcheva E, Hedrich R, et al (2022) Optogenetics for light control of biological systems. Nat Rev Methods Primers 2:55. https://doi.org/10.1038/s43586-022-00136-4

Facomprez A, Beaurepaire E, Débarre D (2012) Accuracy of correction in modal sensorless adaptive optics. Opt Express 20:2598. https://doi.org/10.1364/OE.20.002598

Feng J, Dong H, Lischinsky JE, et al (2024) Monitoring norepinephrine release *in vivo* using next-generation GRABNE sensors. Neuron 112:1930-1942.e6. https://doi.org/10.1016/j.neuron.2024.03.001

Ferlin F (2017) New insights into major theoretical research in optics in the Age of Enlightenment. Centaurus 59:308–319. https://doi.org/10.1111/1600-0498.12163

Fu M, Yu X, Lu J, Zuo Y (2012) Repetitive motor learning induces coordinated formation of clustered dendritic spines *in vivo*. Nature 483:92–95. https://doi.org/10.1038/nature10844

Guo M, Wu Y, Hobson CM, et al (2025) Deep learning-based aberration compensation improves contrast and resolution in fluorescence microscopy. Nat Commun 16:313. https://doi.org/10.1038/s41467-024-55267-x

Hamilton WR (1828) Theory of Systems of Rays. The Transactions of the Royal Irish Academy 15:69–174

Hampson KM, Turcotte R, Miller DT, et al (2021) Adaptive optics for high-resolution imaging. Nat Rev Methods Primers 1:68. https://doi.org/10.1038/s43586-021-00066-7

Hao YA, Lee S, Roth RH, et al (2024) A fast and responsive voltage indicator with enhanced sensitivity for unitary synaptic events. Neuron 112:3680-3696.e8. https://doi.org/10.1016/j.neuron.2024.08.019

Harris KD, Shepherd GMG (2015) The neocortical circuit: themes and variations. Nat Neurosci 18:170–181. https://doi.org/10.1038/nn.3917

Herschel JFW (1833) On the aberrations of compound lenses and object-glasses. Proc R Soc Lond 2:146–147. https://doi.org/10.1098/rspl.1815.0152

Hopkins HH (1951) The concept of partial coherence in optics. Proc R Soc Lond A 208:263–277. https://doi.org/10.1098/rspa.1951.0158

Hu Q, Hailstone M, Wang J, et al (2023) Universal adaptive optics for microscopy through embedded neural network control. Light Sci Appl 12:270. https://doi.org/10.1038/s41377-023-01297-x

Iyer RR, Sorrells JE, Yang L, et al (2022) Label-free metabolic and structural profiling of dynamic biological samples using multimodal optical microscopy with sensorless adaptive optics. Sci Rep 12:3438. https://doi.org/10.1038/s41598-022-06926-w

Ji N, Milkie DE, Betzig E (2010) Adaptive optics via pupil segmentation for high-resolution imaging in biological tissues. Nat Methods 7:141–147. https://doi.org/10.1038/nmeth.1411

Johnson RB (1992) A historical perspective on understanding optical aberrations. Bellingham, United States, p 1026303

Kang I, Kim H, Natan R, et al (2024) Adaptive optical correction for *in vivo* two-photon fluorescence microscopy with neural fields

Karpf S, Riche CT, Di Carlo D, et al (2020) Spectro-temporal encoded multiphoton microscopy and fluorescence lifetime imaging at kilohertz frame-rates. Nat Commun 11:2062. https://doi.org/10.1038/s41467-020-15618-w

Kazemipour A, Novak O, Flickinger D, et al (2019) Kilohertz frame-rate two-photon tomography. Nat Methods 16:778–786. https://doi.org/10.1038/s41592-019-0493-9

Kleinfeld D, Blinder P, Drew PJ, et al (2011) A guide to delineate the logic of neurovascular signaling in the brain. Front Neuroenerg 3:. https://doi.org/10.3389/fnene.2011.00001

Lai QTK, Yip GGK, Wu J, et al (2021) High-speed laser-scanning biological microscopy using FACED. Nat Protoc 16:4227–4264. https://doi.org/10.1038/s41596-021-00576-4

Lee DJ, Welsh BM, Roggemann MC, Ellerbroek BL (1997) Diagnosing unknown aberrations in an adaptive optics system by use of phase diversity. Opt Lett 22:952. https://doi.org/10.1364/OL.22.000952

Liu R, Li Z, Marvin JS, Kleinfeld D (2019) Direct wavefront sensing enables functional imaging of infragranular axons and spines. Nat Methods 16:615–618. https://doi.org/10.1038/s41592-019-0434-7

Liu Z, Lu X, Villette V, et al (2022) Sustained deep-tissue voltage recording using a fast indicator evolved for two-photon microscopy. Cell 185:3408-3425.e29. https://doi.org/10.1016/j.cell.2022.07.013

Manley J, Lu S, Barber K, et al (2024) Simultaneous, cortex-wide dynamics of up to 1 million neurons reveal unbounded scaling of dimensionality with neuron number. Neuron 112:1694-1709.e5. https://doi.org/10.1016/j.neuron.2024.02.011

Marshel JH, Kim YS, Machado TA, et al (2019) Cortical layer–specific critical dynamics triggering perception. Science 365:eaaw5202. https://doi.org/10.1126/science.aaw5202

Milkie DE, Betzig E, Ji N (2011) Pupil-segmentation-based adaptive optical microscopy with full-pupil illumination. Opt Lett 36:4206. https://doi.org/10.1364/OL.36.004206

Nasu Y, Aggarwal A, Le GNT, et al (2023) Lactate biosensors for spectrally and spatially multiplexed fluorescence imaging. Nat Commun 14:6598. https://doi.org/10.1038/s41467-023-42230-5

Papagiakoumou E, Anselmi F, Bègue A, et al (2010) Scanless two-photon excitation of channelrhodopsin-2. Nat Methods 7:848–854. https://doi.org/10.1038/nmeth.1505

Patriarchi T, Cho JR, Merten K, et al (2018) Ultrafast neuronal imaging of dopamine dynamics with designed genetically encoded sensors. Science 360:eaat4422. https://doi.org/10.1126/science.aat4422

Platisa J, Ye X, Ahrens AM, et al (2023) High-speed low-light *in vivo* two-photon voltage imaging of large neuronal populations. Nat Methods 20:1095–1103. https://doi.org/10.1038/s41592-023-01820-3

Prosser RB (1917) The invention of the achromatic lens. The Observatory 40:297–301

Qin Z, Chen C, He S, et al (2020) Adaptive optics two-photon endomicroscopy enables deep-brain imaging at synaptic resolution over large volumes. Sci Adv 6:eabc6521. https://doi.org/10.1126/sciadv.abc6521

Rocha JCA, Wright T, Būtaitė UG, et al (2024) Fast and light-efficient wavefront shaping with a MEMS phase-only light modulator. Opt Express 32:43300. https://doi.org/10.1364/OE.541857

Rodríguez C, Chen A, Rivera JA, et al (2021) An adaptive optics module for deep tissue multiphoton imaging *in vivo*. Nat Methods 18:1259–1264. https://doi.org/10.1038/s41592-021-01279-0

Rueckel M, Mack-Bucher JA, Denk W (2006) Adaptive wavefront correction in two-photon microscopy using coherence-gated wavefront sensing. Proc Natl Acad Sci USA 103:17137–17142. https://doi.org/10.1073/pnas.0604791103

Russell LE, Dalgleish HWP, Nutbrown R, et al (2022) All-optical interrogation of neural circuits in behaving mice. Nat Protoc 17:1579–1620. https://doi.org/10.1038/s41596-022-00691-w

Sabatini BL, Tian L (2020) Imaging Neurotransmitter and neuromodulator dynamics *in vivo* with genetically encoded indicators. Neuron 108:17–32. https://doi.org/10.1016/j.neuron.2020.09.036

Sims RR, Bendifallah I, Grimm C, et al (2024) Scanless two-photon voltage imaging. Nat Commun 15:5095. https://doi.org/10.1038/s41467-024-49192-2

Streich L, Boffi JC, Wang L, et al (2021) High-resolution structural and functional deep brain imaging using adaptive optics three-photon microscopy. Nat Methods 18:1253–1258. https://doi.org/10.1038/s41592-021-01257-6

Tang J, Germain RN, Cui M (2012) Superpenetration optical microscopy by iterative multiphoton adaptive compensation technique. Proc Natl Acad Sci USA 109:8434–8439. https://doi.org/10.1073/pnas.1119590109

Wang C, Liu R, Milkie DE, et al (2014) Multiplexed aberration measurement for deep tissue imaging *in vivo*. Nat Methods 11:1037–1040. https://doi.org/10.1038/nmeth.3068

Wang K, Sun W, Richie CT, et al (2015) Direct wavefront sensing for high-resolution *in vivo* imaging in scattering tissue. Nat Commun 6:7276. https://doi.org/10.1038/ncomms8276

Wright WJ, Hedrick NG, Komiyama T (2025) Distinct synaptic plasticity rules operate across dendritic compartments *in vivo* during learning. Science 388:322–328. https://doi.org/10.1126/science.ads4706

Wu J, Liang Y, Chen S, et al (2020) Kilohertz two-photon fluorescence microscopy imaging of neural activity *in vivo*. Nat Methods 17:287–290. https://doi.org/10.1038/s41592-020-0762-7

Wu J-L, Xu Y-Q, Xu J-J, et al (2016) Ultrafast laser-scanning time-stretch imaging at visible wavelengths. Light Sci Appl 6:e16196–e16196. https://doi.org/10.1038/lsa.2016.196

Xiao S, Davison I, Mertz J (2021) Scan multiplier unit for ultrafast laser scanning beyond the inertia limit. Optica 8:1403. https://doi.org/10.1364/OPTICA.445254

Yang Y, Li B, Li Y (2024) Genetically encoded sensors for the *in vivo* detection of neurochemical dynamics. Annual Review of Analytical Chemistry 17:367–392. https://doi.org/10.1146/annurev-anchem-061522-044819

Yao P, Liu R, Broggini T, et al (2023) Construction and use of an adaptive optics two-photon microscope with direct wavefront sensing. Nat Protoc 18:3732–3766. https://doi.org/10.1038/s41596-023-00893-w

Yu X, Todi A, Tang H (2018) Bessel beam generation using a segmented deformable mirror. Appl Opt 57:4677. https://doi.org/10.1364/AO.57.004677

Zernike VF (1934) Beugungstheorie des schneidenver-fahrens und seiner verbesserten form, der phasenkontrastmethode. Physica 1:689–704. https://doi.org/10.1016/S0031-8914(34)80259-5

Zhang P, Ma D, Cheng X, et al (2023a) Deep learning-driven adaptive optics for single-molecule localization microscopy. Nat Methods 20:1748–1758. https://doi.org/10.1038/s41592-023-02029-0

Zhang Q, Yang Y, Cao KJ, et al (2023b) Retinal microvascular and neuronal pathologies probed *in vivo* by adaptive optical two-photon fluorescence microscopy. eLife 12:e84853. https://doi.org/10.7554/eLife.84853

Zhang Y, Rózsa M, Liang Y, et al (2023c) Fast and sensitive GCaMP calcium indicators for imaging neural populations. Nature 615:884–891. https://doi.org/10.1038/s41586-023-05828-9

Zhuo Y, Luo B, Yi X, et al (2024) Improved green and red GRAB sensors for monitoring dopaminergic activity *in vivo*. Nat Methods 21:680–691. https://doi.org/10.1038/s41592-023-02100-w

FIGURE CAPTIONS

Figure 1. Methods for accelerating scan rate. (A) Traditional galvanometer scanning, (B) scan rate multiplication units (SMUs), (C) reverberation cavity, (D) spatiotemporal multiplexed ultrafast resonance frame-scanning (SMURF), (E) free-space angular-chirp-enhanced dela (FACED), (F) Scanless two-photon microscopy (F) spectro-temporal laser imaging by diffractive excitation (SLIDE), and (G) scanned line angular projection (SLAP) microscopy.

Figure 2. Principles of Fourier optics. (A) Relationship between the optical field at two planes on either side of an optical element with a transfer function of $H(x,y)$ at a distance *d* apart from a lens. (B) Illustration of the Fourier transforming capability of a lens, using a mirror tilted at an angle at the back focal plane that creates a displacement along the focal plane. (C-D) Effect to the wavefront from sample-induced optical aberrations (C) and how AO using wavefront reshaping can restore the focus into the sample (D).

Figure 3. Principles of wavefront actuators and sensors. (A) Segmented deformable mirrors (discrete mirror elements for fast, coarse aberration correction), and (B) Continuous deformable mirrors (smooth surface deformations for fine, high fidelity correction) of tissue induced distortions during deep brain imaging. (C) Liquid crystal SLMs impose programmable phase shifts by voltage driven alignment of liquid crystal molecules, enabling flexible aberration correction and holographic beam shaping for advanced optical neuroimaging (D) The Shack Hartmann sensor measures optical aberrations by passing the wavefront through a microlens array, which divides the incoming light into multiple sub aperture beams A planar (aberration free) wavefront (produces a regular grid of focal spots, whereas an aberrated wavefront (causes spot displacements proportional to the local phase gradients By calculating these shifts, the system reconstructs the aberration map of the incoming light.

Figure 4. Illustration of Zernike polynomial wavefront phase (top) and subsequent PSF at the sample (bottom) for the first 28 polynomials (up to 6th order).

Figure 5. System diagram for the AO 2P microscope's excitation path. (A) and wavefront detection path (B), with the numbered elements showing the order for alignment. The conjugate sample planes and the Fourier planes (pupil planes) are also labelled to trace the 4-*f* relays within the setup.

Figure 6. Two-photon absorption cross-section of Cy5.5 dextran. The Cy5.5 samples were prepared in deuterated DMSO. Corrected two-photon excitation spectra were measured according to the methods described previously (Drobizhev et al. 2020). The two-photon cross sections were measured by a relative method, where

fluorescence signals were measured under two- and one-photon excitation of diluted solutions of the sample and reference, see (Dalangin et al. 2025). Rhodamine B in alkaline ethanol was used as a reference standard at 1064 nm.

Figure 7. Evaluation of image metrics for AO-2P imaging while imaging tdTomato-labelled somatostatin-expressing neurons in the mouse somatosensory cortex at 55 depths between 670-690 µm below the pial surface. **A.** Maximum intensity projection across a 10-µm region with system-only aberration correction (Sys AO) and the full AO with the wavefront detected from Cy5.5 labeling (Full AO). **B.** Cross-section along the two lines indicated in A, showing fine structures apparent after correction. **C.** Spectral power as a function of spatial frequency k for the images in A. **D.** The image metric $\mathbf{y_m}$ showing the sum of the 512 brightest pixels in the image before and after correction. **E-I.** The calculated RMS contrast, SNR, SBR, CNR, and PBR at each depth. **J.** The histogram of intensity distribution at each depth (average of 100 acquired frames) before and after correction. **K.** |k|-space plot of the average magnitude of the spatial frequency for the depths with system AO and full AO correction. **L.** The HFFM calculated for each depth before and after correction.

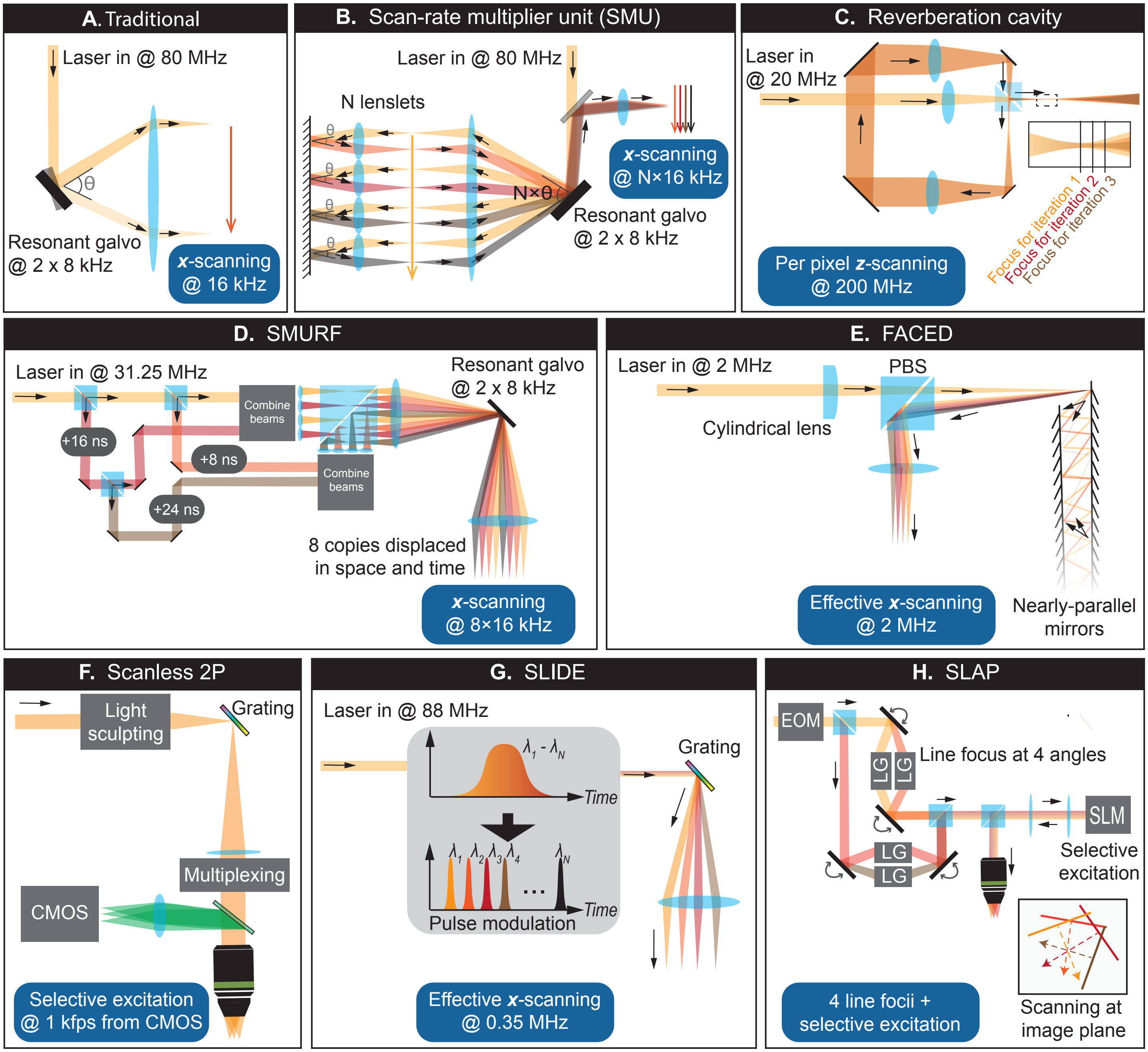

Figure 1 - Iyer, Yao, Drobizhev, Nezhad, Nguyen, Chung and Kleinfeld

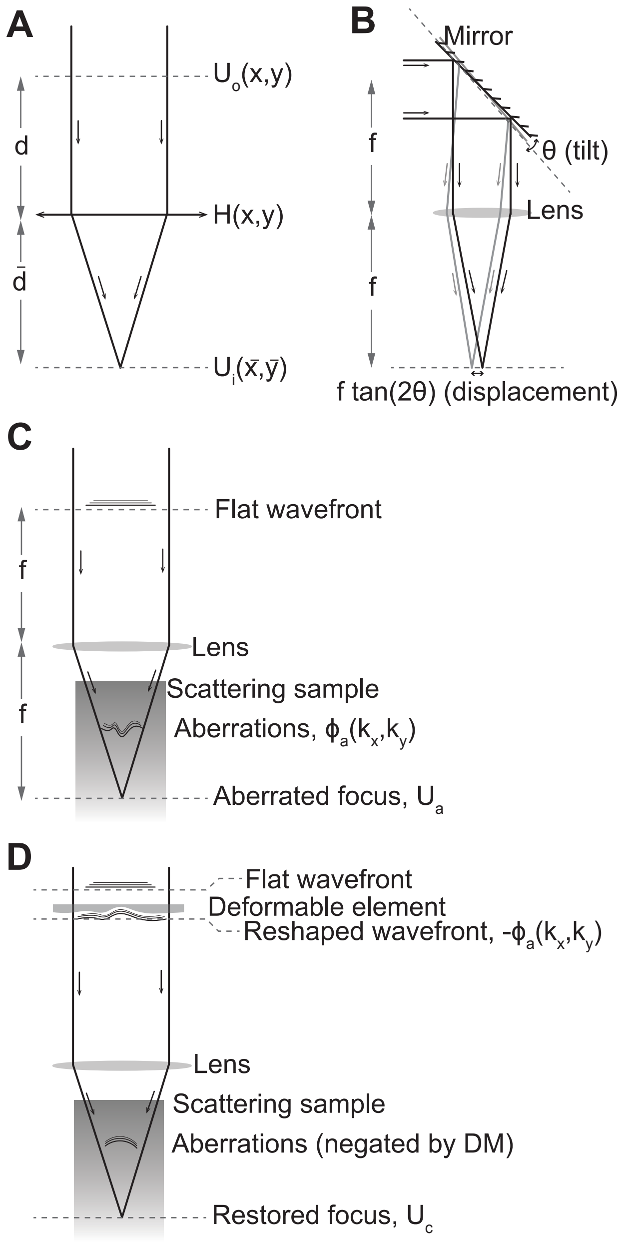

Figure 2 - Iyer, Yao, Drobizhev, Nezhad, Nguyen, Chung and Kleinfeld

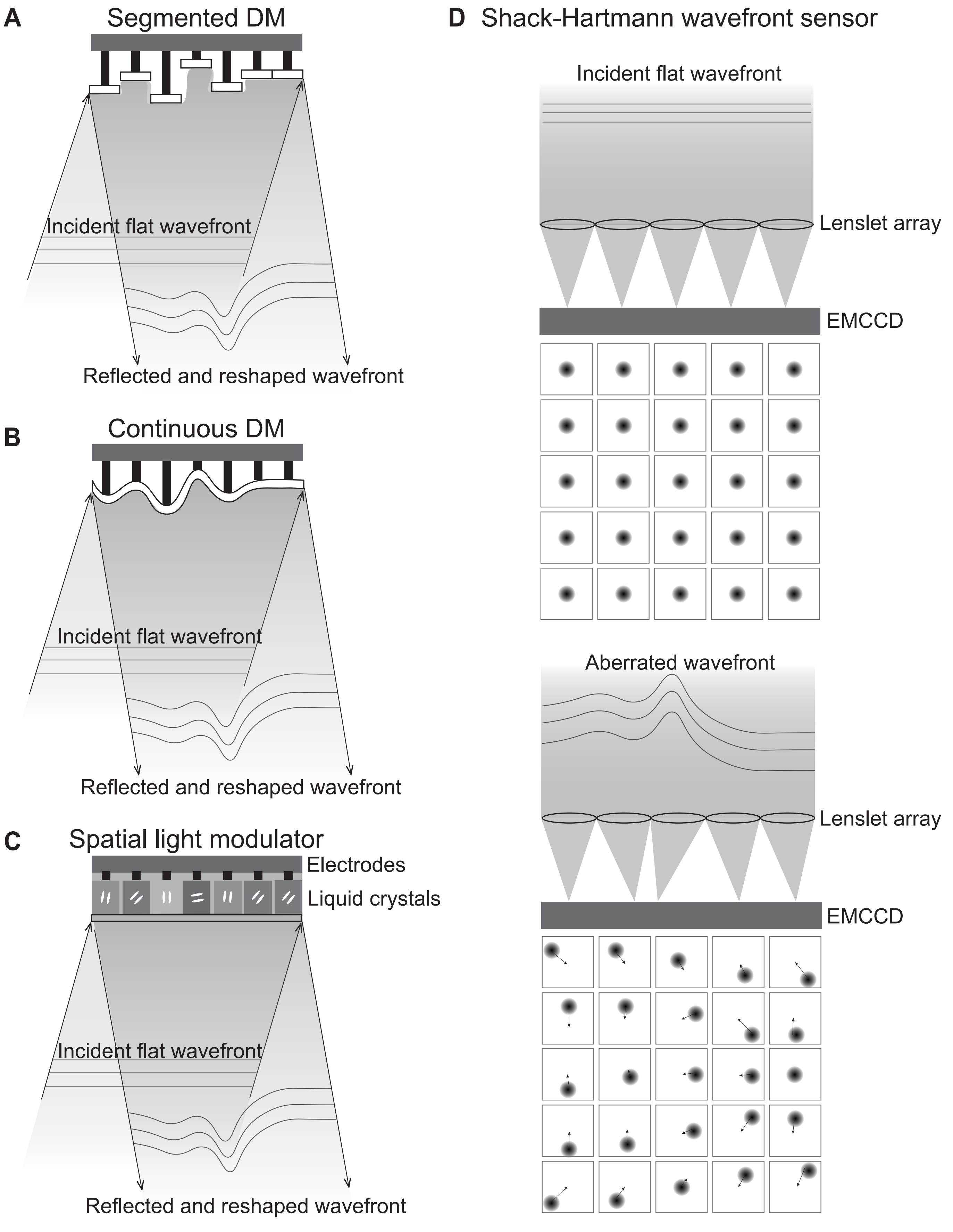

Figure 3 - Iyer, Yao, Drobizhev, Nezhad, Nguyen, Chung and Kleinfeld

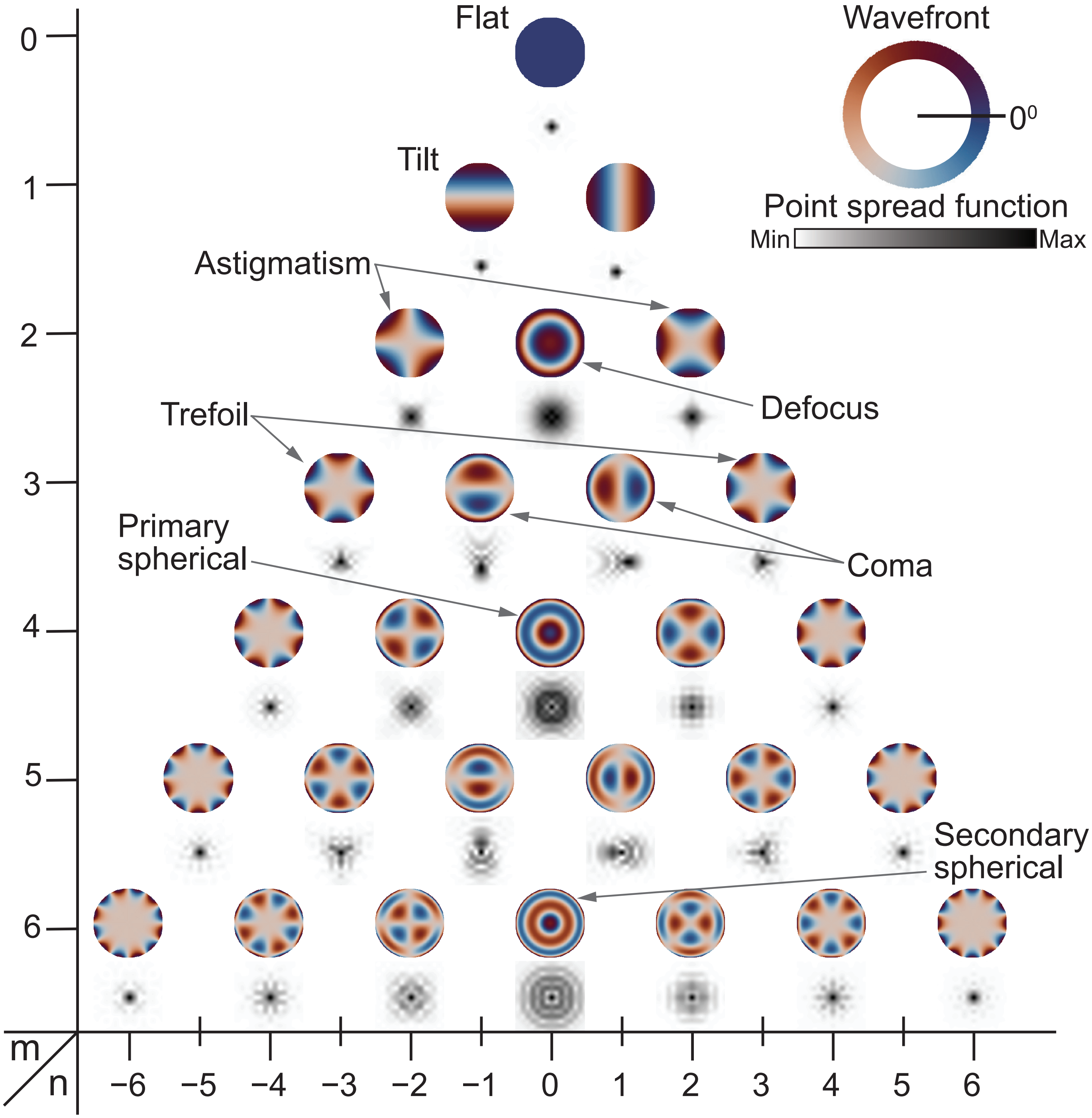

Figure 4 - Iyer, Yao, Drobizhev, Nezhad, Nguyen, Chung and Kleinfeld

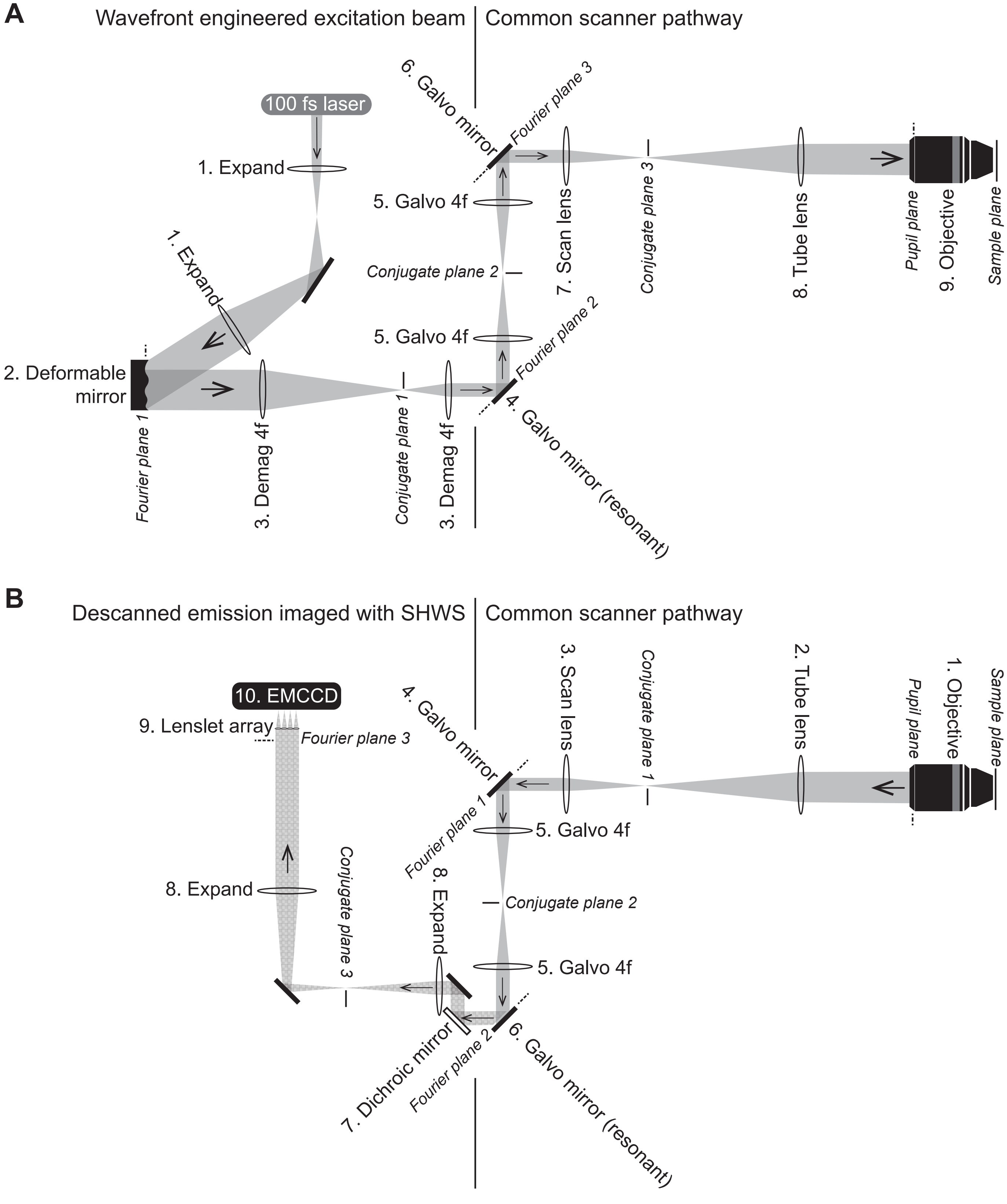

Figure 5 - Iyer, Yao, Drobizhev, Nezhad, Nguyen, Chung and Kleinfeld

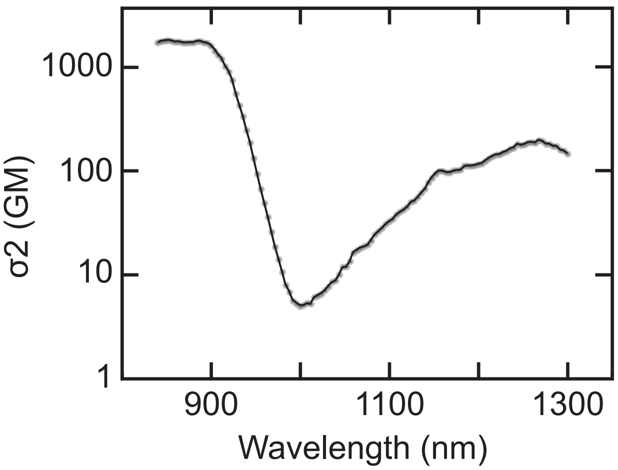

Figure 6 - Iyer, Yao, Drobizhev, Nezhad, Nguyen, Chung and Kleinfeld

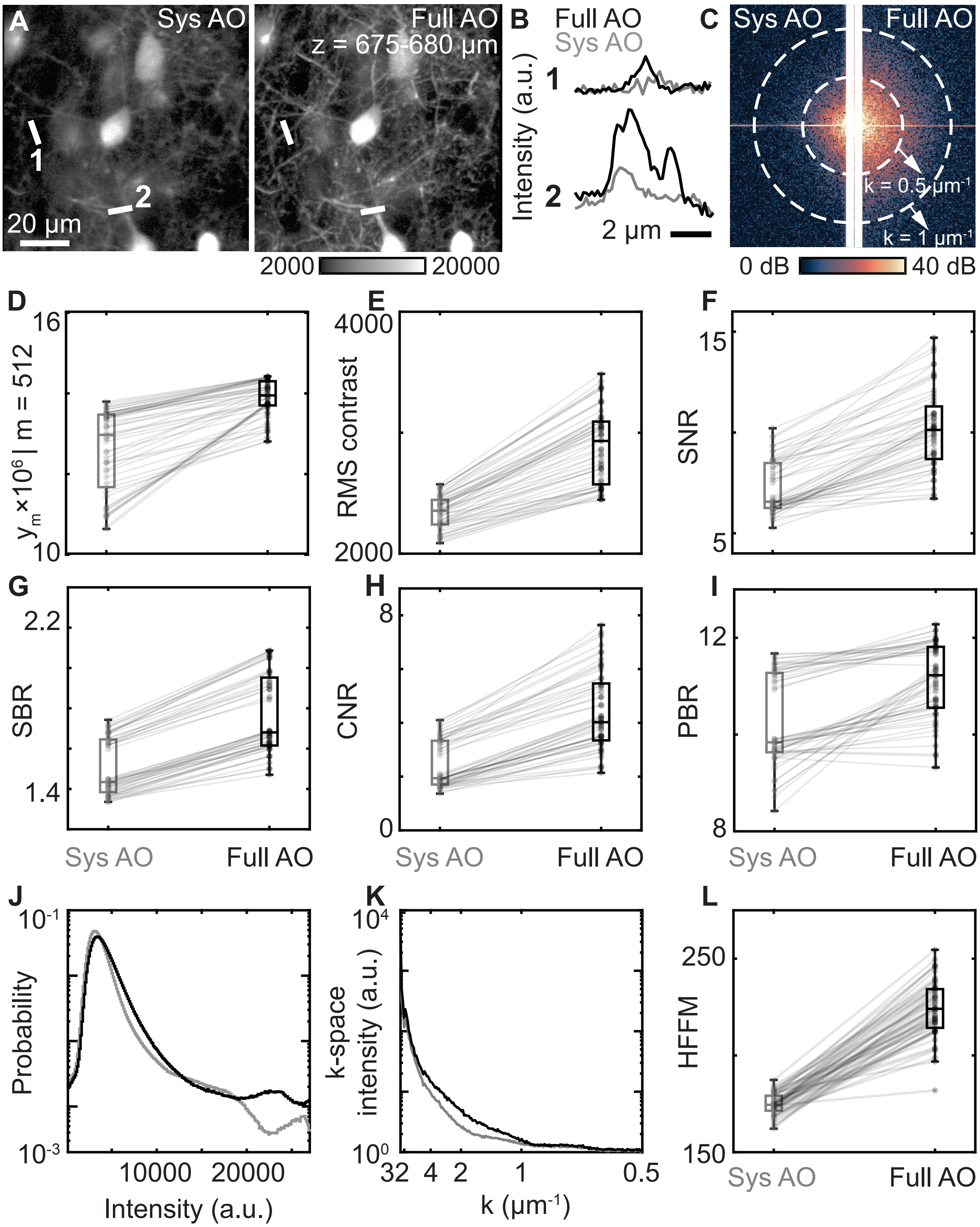

Figure 7 - Iyer, Yao, Drobizhev, Nezhad, Nguyen, Chung and Kleinfeld